J. Fluid Mech. (2002), *vol.* 466, *pp.* 17–52.
DOI: 10.1017/S0022112002001179 Printed in the United Kingdom

Dynamics of homogeneous bubbly flows Part 1. Rise velocity and microstructure of the bubbles

By BERNARD BUNNER[1] AND GRÉTAR TRYGGVASON[2]

[1]Coventor, Inc., Cambridge, MA 02138, USA

[2]Mechanical Engineering Department, Worcester Polytechnic Institute, Worcester, MA 01609-2280, USA

(Received 14 March 2000 and in revised form 5 March 2002)

Direct numerical simulations of the motion of up to 216 three-dimensional buoyant bubbles in periodic domains are presented. The full Navier–Stokes equations are solved by a parallelized finite-difference/front-tracking method that allows a deformable interface between the bubbles and the suspending fluid and the inclusion of surface tension. The governing parameters are selected such that the average rise Reynolds number is about 12–30, depending on the void fraction; deformations of the bubbles are small. Although the motion of the individual bubbles is unsteady, the simulations are carried out for a sufficient time that the average behaviour of the system is well defined. Simulations with different numbers of bubbles are used to explore the dependence of the statistical quantities on the size of the system. Examination of the microstructure of the bubbles reveals that the bubbles are dispersed approximately homogeneously through the flow field and that pairs of bubbles tend to align horizontally. The dependence of the statistical properties of the flow on the void fraction is analysed. The dispersion of the bubbles and the fluctuation characteristics, or 'pseudo-turbulence', of the liquid phase are examined in Part 2.

1. Introduction

Bubbly flows have been studied for a long time. Although the dynamics of a single bubble has attracted considerable attention and is now well understood, many practical applications require predictions of the behavior of a large number of bubbles. Examples include boiling flows, bubble columns for diverse chemical processes, air entrainment at the air/ocean interface, and many others. Engineering predictions of multiphase flows rely on conservation equations for the averaged properties of the mixture and closure laws to relate subgrid processes to the averaged behavior of the system.

For turbulent flows, direct numerical simulations, where the unsteady Navier–Stokes equations are solved on grids fine enough to fully resolve all flow scales, have had a major impact on the current understanding of turbulence in single-phase flows. In two-phase flows, additional complexity arises from the presence of a second phase with significantly different physical properties. The need for direct numerical simulations in the study of multiphase flows has been apparent for some time. However, the challenge of simulating the unsteady motion of moving fluid interfaces has led investigators to use simplified models. For dispersed flows, where bubbles,

drops or solid particles of one phase move within another continuous phase, assuming Stokes flow (Pozrikidis 1993; Loewenberg & Hinch 1996), potential flow (Sangani & Didwania 1993; Smereka 1993), or point particles (Squires & Eaton 1990; Elghobashi & Truesdell 1992; Wang & Maxey 1993) are typical examples of such simplifications. Direct numerical simulations, in which the flow is completely resolved, are very recent.

Esmaeeli & Tryggvason (1996, 1998) used direct numerical simulations to examine the motion of a number of freely evolving bubbles at low yet finite Reynolds numbers (around 1–2, depending on volume fraction and dimensionality). The simulations were done using periodic domains and included up to 324 two-dimensional bubbles and 8 three-dimensional ones. The simulations showed that a regular array is unstable and that it breaks up through two-bubble interactions of the 'drafting, kissing, and tumbling' type. Although the motion of a regular array at $O(1)$ Reynolds numbers is fairly similar to Stokes flow, the evolution of the free array differs by the strong two-bubble interactions. In Esmaeeli & Tryggvason (1999), the evolution was examined at a higher Reynolds number (around 20–30 for the lowest volume fraction). For the low Reynolds numbers, the freely evolving array rose faster than the regular one, in agreement with Stokes flow predictions, but at the higher Reynolds number the freely evolving array rose slower than the regular one. The effect of the number of bubbles in each period was examined for the two-dimensional system and it was found that the rise Reynolds number and the velocity fluctuations in the liquid (the Reynolds stresses) generally increase with the size of the system. While some aspects of the fully three-dimensional flows, such as the dependence of the rise velocity on the Reynolds number, are predicted by results for two-dimensional flows, the structure of the bubble distribution and the magnitude of the Reynolds stresses are not. For references to other computations of bubble motions, see Esmaeeli & Tryggvason (1998, 1999). For solid particles, Glowinski *et al.* (1999) have performed calculations of up to 504 particles in two dimensions. The results reported here include a much larger number of bubbles than those presented by Esmaeeli & Tryggvason and were obtained by a parallel code using the same methodology. This paper focuses on the rise velocity and the microstructure of the bubbles while Bunner & Tryggvason (2002*a*), henceforth referred to as Part 2, focuses on the fluctuations of the bubbles and the liquid.

2. Problem statement and numerical method

We consider the three-dimensional motion of a triply periodic monodisperse array of buoyant bubbles with equivalent diameter d or radius a, density ρ_b, viscosity μ_b, and uniform surface tension σ in a fluid with density ρ_f and viscosity μ_f. The array of bubbles is repeated periodically in the three spatial directions with periods equal to L. In addition to the acceleration due to gravity, $\boldsymbol{g}$, a uniform acceleration is imposed on the fluid inside and outside the bubbles to compensate for the hydrostatic head, so that the net momentum flux through the boundaries of the computational domain is zero. This is explained in more detail in § 2.1.

A single bubble of light fluid rising in an unbounded flow is usually described by the Eötvös number (sometimes also called Bond number), $Eo = \rho_f g d^2/\sigma$ and the Morton number, $M = g\mu_f{}^4/\rho_f\sigma^3$ (see Clift, Grace & Weber 1978). For given fluids, the Eötvös number is a characteristic of the bubble size and the Morton number is a constant. Instead of the Morton number, we prefer to use the Galileo or Archimedes number, $N = \rho^2 g d^3/\mu^2 = Eo^{3/2}/M^{1/2}$, which is a Reynolds number squared based on the velocity scale $(gd)^{1/2}$. In this paper, we choose $Eo = 1$ and $N = 900$ ($M = 1.2345 \times 10^{-6}$). This Morton number corresponds to a light machine

oil at a temperature of about 65 °C ($\mu_f = 0.0131\,\mathrm{N\,s\,m^{-2}}$, $\rho_f = 880\,\mathrm{kg\,m^{-3}}$, $\sigma = 0.03\,\mathrm{N\,m^{-1}}$, and $g = 9.81\,\mathrm{m\,s^{-2}}$) and the Eötvös number corresponds to a bubble with a diameter of about 1.9 mm. For the somewhat more interesting case of an air bubble in water, the Galileo number is usually much higher, but current computational capabilities make the study of a three-dimensional system of many bubbles in water very difficult. The fluids are taken to be free of contaminants in the simulations. The ratios of the densities and viscosities, ρ_b/ρ_f and μ_b/μ_f, are two additional dimensionless parameters. These ratios are very small in most bubbly flows (the density ratio for air bubbles in water is 1/1000, for example). For computational reasons discussed in § 2.7, the simulations were performed at a higher value, $\rho_b/\rho_f = \mu_b/\mu_f = 1/50$. It is shown in § 2.7 that this approximation has a small effect on the results.

At the initial time, the N_b bubbles are placed inside the periodic cell corresponding to the computational domain, and arranged in a regular array, which is perturbed slightly in each direction in a manner described in § 3. The initial configuration of the bubbles has little effect on the results, as explained in § 3. As they rise, the bubbles move into the other periodic cells in the vertical direction through buoyancy and in the horizontal direction through dispersion. The bubbles are not allowed to coalesce, so that N_b is constant. A fifth dimensionless parameter for this problem is the void fraction, or volume fraction of the bubbly phase, $\alpha = N_b \pi d^3/6L^3$. Since both fluids are assumed to be incompressible, α is constant throughout a simulation. In this paper, values of α ranging from 2% to 24% are considered, corresponding respectively to dilute and dense flows. The number of bubbles, N_b, is an additional parameter, and its effect is studied by looking at systems with $N_b = 1$, 2, 4, 12, 27, 91 and 216 at $\alpha = 6\%$ and with $N_b = 1$, 27, and 54 at $\alpha = 12\%$. It is found that the rise velocity depends only weakly on N_b when $N_b \geqslant 12$, while the velocity fluctuations and dispersion characteristics of the bubbles and the 'pseudo-turbulence' of the liquid are shown in Part 2 to be significantly affected by N_b.

2.1. *One-field formulation of the Navier–Stokes equations*

The fluids inside and outside the bubbles are taken to be Newtonian and the flow is taken to be incompressible and isothermal, so that densities and viscosities are constant within each phase. The velocity field is solenoidal:

$$\nabla \cdot \boldsymbol{u} = 0. \tag{2.1}$$

A single Navier–Stokes equation with variable density ρ and viscosity μ is solved for the entire computational domain Ω. The momentum equation in conservative form is

$$\frac{\partial \rho \boldsymbol{u}}{\partial t} + \nabla \cdot \rho \boldsymbol{u}\boldsymbol{u} = -\nabla P + (\rho - \rho_0)\boldsymbol{g} + \nabla \cdot \mu(\nabla \boldsymbol{u} + \nabla^T \boldsymbol{u}) + \int \sigma \kappa' \boldsymbol{n}' \delta^\beta(\boldsymbol{x} - \boldsymbol{x}')\,\mathrm{d}A', \tag{2.2}$$

where $\boldsymbol{u}$ is the velocity, p the pressure, $\boldsymbol{g}$ the acceleration due to gravity, and σ the constant surface tension. An additional body force defined by $\rho_0 \boldsymbol{g}$, where $\rho_0 = \alpha\rho_b + (1-\alpha)\rho_f$ is the mean density, is imposed on both fluids and ensures that the net momentum flux through the boundaries of the domain $\partial\Omega$ is zero, $\int_{\partial\Omega} \rho \boldsymbol{u} = 0$. This term is analogous to the pressure gradient generated by the base of a flow container, which balances the total gravitational force on the fluid (Ladd 1997). In its absence, gravity would cause the entire flow field to accelerate in the downward vertical direction since all boundary conditions are periodic and there are no walls. The last term in equation (2.2) accounts for surface tension at the front: κ' is twice the mean local curvature of the front, $\boldsymbol{n}'$ is the unit vector normal to the front, and

$\mathrm{d}A'$ is the area element on the front; $\delta^\beta(\boldsymbol{x}-\boldsymbol{x}')$ is a three-dimensional δ-function constructed by repeated multiplication of one-dimensional δ-functions, where $\boldsymbol{x}$ is the point at which the equation is evaluated and $\boldsymbol{x}'$ is a point on the front. This delta function represents the discontinuity of the stresses across the interface, while the integral over the front expresses the smoothness of the surface tension along the interface. By integrating equations (2.1) and (2.2) over a small volume enclosing the interface and making this volume shrink, it is possible to show that the velocities and tangential stresses are continuous across the interface and that the usual statement of normal stress discontinuity at the interface is recovered:

$$[-P+\mu(\nabla\boldsymbol{u}+\nabla^T\boldsymbol{u})]\boldsymbol{n}=\sigma\kappa\boldsymbol{n}, \tag{2.3}$$

where the brackets denote the jump across the interface.

2.2. *Finite difference/front tracking method*

Equation (2.2) is discretized in space by centred finite differences on a uniform staggered grid with n_x, n_y and n_z grid points in each direction. A projection method plus a predictor–corrector method are employed for discretization in time. The numerical scheme is therefore second-order accurate in space and in time.

The two major challenges of simulating interfaces between different fluids are to maintain a sharp front and to compute the surface tension accurately. In this paper, we use a front tracking method originally developed by Unverdi & Tryggvason (1992) and improved by Esmaeeli & Tryggvason (1998). The main features of the method are presented briefly here; a complete description is available in Tryggvason *et al.* (2001). In addition to the three-dimensional fixed grid on which the Navier–Stokes equation is solved, a moving, deformable two-dimensional mesh is used to track the boundary between the bubble and the ambient fluid. This mesh consists of marker points connected by triangular elements.

The advection of the density on the fixed grid between time steps n and $n+1$ is accomplished by first moving the front and then constructing a grid-density field to match the location of the front. The velocity of each front marker point is interpolated from the fluid velocities at the four grid nodes surrounding the front point in each direction using the weighting functions proposed by Peskin (1977). After all points have been advected, a discrete version of the density gradient across each front element, written symbolically as $\nabla_h\rho=(\rho_b-\rho_f)\int\delta_h\boldsymbol{n}\,\mathrm{d}A'$, is calculated on the front and distributed onto the grid; δ_h is a discrete delta function and is defined on a compact support of 4^3 grid points with the same weighting functions suggested by Peskin. A smooth density field is then obtained by solving the following Poisson equation:

$$\nabla_h^2\rho=\nabla_h\cdot\nabla_h\rho. \tag{2.4}$$

Instead of a sharply discontinuous density field, the density jump from ρ_b to ρ_f is smoothed over an interval of about 4 grid points in each spatial direction. The viscosity field is derived by affine scaling from the density field.

Because it is necessary to simulate the motion of the bubbles over long periods of time in order to obtain statistical steady-state results, an accurate and robust technique for the calculation of the surface tension is critical. This is achieved by converting the surface integral of the curvature over the area of a triangular element ΔS into a contour integral over the edges $\partial\Delta S$ of this element. The local surface

tension $\Delta \boldsymbol{F}_e$ on this element is then:

$$\Delta \boldsymbol{F}_e = \sigma \int_{\Delta S} \kappa \boldsymbol{n} \, \mathrm{d}A = \sigma \int_{\partial \Delta S} \boldsymbol{t} \times \boldsymbol{m} \, \mathrm{d}l, \tag{2.5}$$

where $\boldsymbol{n}$ is the unit vector normal to the element surface, and $\boldsymbol{t}$ and $\boldsymbol{m}$ are the unit vectors in the plane tangent to the element, which are respectively tangent and normal to the edges of the element. Vectors $\boldsymbol{t}$ and $\boldsymbol{m}$ are found by fitting a paraboloid surface through the three vertices of the triangle ΔS and the three other vertices of the three adjacent elements. To ensure that $\boldsymbol{t}$ and $\boldsymbol{m}$ on the common edge of two neighbouring elements are identical, they are replaced by their averages. As a consequence, the integral of the surface tension over each bubble remains zero throughout its motion. Even small errors in the evaluation of the surface tension can result in a net force that might, for example, cause a single bubble in an unbounded domain to migrate in the lateral direction. The final step is to distribute the surface tension onto the fixed grid in the same manner as the density gradient.

As a bubble moves, front points and elements accumulate at the rear of the bubble, while depletion occurs at the top of the bubble. It is therefore necessary to add and delete points and elements in order to maintain adequate local resolution on the front. The criteria for adding and deleting points and elements are based on the length of the edges of the elements and on the magnitude of the angles of the elements; more details of the restructuring algorithm are given in Tryggvason *et al.* (2001). Typically about 1% of the points and elements are added or deleted at each time step.

Although it is possible to allow two bubbles to coalesce when they come close to each other (see Nobari, Jan & Tryggvason 1996, for an example of colliding drops), this is not done in this paper. There are two reasons for this. First of all, we are interested in the average properties of the steady state and it is undesirable if the number and size of the bubbles changed as the simulation progressed. The second reason is that we believe that it is difficult, at the present time, to implement coalescence into the code in a physical way. Actual coalescence should not take place until the film between the bubbles is much smaller than the smallest resolved distance. In simulations using marker functions to follow the phase boundary, such as volume-of-fluid or level-set methods, the bubbles fuse together as soon as the distance between them is smaller than a grid space. This makes the coalescence dependent on the resolution and is clearly undesirable. The present computations lead to essentially fully converged results, even if the film between the bubbles is not fully resolved, since the flow in the film is a simple plug flow (Qian 1997). At the lowest volume fraction for spherical bubbles, collisions between the bubbles are relatively rare, so our assumption should be a good approximation of reality.

In summary, the sequence of operations performed to move the flow field from time step n to time step $n+1$ is as follows. First the front is advected using the velocity field at n. From the new position of the front at $n+1$, the density and viscosity fields are reconstructed and the surface tension is calculated on the front and transferred to the fixed grid. The convective, viscous, and gravitational terms are calculated using the density, viscosity and velocity fields at time step n and added to the surface tension to give an unprojected velocity field $\boldsymbol{u}^\star$. Combining equations (2.1) and (2.2) results in a non-separable elliptic equation for the pressure:

$$\nabla \frac{1}{\rho^{n+1}} \cdot \nabla P = \frac{1}{\Delta t} \nabla \cdot \boldsymbol{u}^\star. \tag{2.6}$$

This equation ensures that the velocity field at time $n+1$, $\boldsymbol{u}^{n+1}$, which is derived from

P and $\boldsymbol{u}^{\star}$, is solenoidal. The operations described above represent the first step of the predictor–corrector method. They are repeated and the results are averaged with the values at time step n to yield the velocity field and front position at time step $n+1$.

The front-tracking method does not explicitly conserve the volume of the bubbles. The following technique was developed to ensure that the volume of the bubbles remains constant. The volume error ΔVol_b is calculated at every time step for each bubble. If it exceeds a small threshold, typically 0.1% of the original volume, the coordinates of the front points on the bubble are adjusted according to

$$\boldsymbol{OM}' = \boldsymbol{OM} - \Delta Vol_b \frac{\boldsymbol{OM}\cdot\boldsymbol{n}}{4\pi\|\boldsymbol{OM}\|^3}\boldsymbol{n}. \tag{2.7}$$

Here $\boldsymbol{O}$ is the centroid of the bubble, $\boldsymbol{n}$ is the unit vector normal to the front pointing out of the bubble, and $\boldsymbol{M}$ and $\boldsymbol{M}'$ are the positions of a front point before and after correction. This correction algorithm amounts to adding a potential sink of volume at the centroid of the bubble and is typically applied every 100 time steps. A similar technique is used by Zhou & Pozrikidis (1993) to compensate for volume changes in a boundary integral method.

The numerical method was parallelized for distributed-memory parallel computers and a parallel multigrid solver was developed to accelerate the solution of the Poisson equations for the density, equation (2.4), and the pressure, equation (2.6). More details of the parallelization are available in Bunner & Tryggvason (1999) and Bunner (2000).

2.3. *Definition of the bubble velocities, fluctuation velocities and fluid turbulence quantities*

The velocity field $\boldsymbol{v} = (u, v, w)$ is defined as $\boldsymbol{v}_b = (u_b, v_b, w_b)$ in the bubbly phase and $\boldsymbol{v}_f = (u_f, v_f, w_f)$ in the liquid phase. The volume-averaged velocities of the bubbly phase and of the liquid phase are $\boldsymbol{V}_b = \langle \boldsymbol{v}_b \rangle = (U_b, V_b, W_b)$ and $\boldsymbol{V}_f = \langle \boldsymbol{v}_b \rangle = (U_f, V_f, W_f)$. The relative or slip velocity between the two phases is $\boldsymbol{V}_r = \boldsymbol{V}_b - \boldsymbol{V}_f$.

Since the surface of the bubble is tracked explicitly, it is advantageous to use the marker points to calculate the location and velocity of the bubbles. The volume integrals are transformed into surface integrals using the divergence theorem. The volume $Vol_b^{(l)}$ and centroid position $\boldsymbol{r}_b^{(l)}$ of bubble l are

$$Vol_b^{(l)} = \int_{Vol_b^{(l)}} \mathrm{d}V = \frac{1}{3}\int_{Vol_b^{(l)}} \nabla\cdot\boldsymbol{r}\,\mathrm{d}V = \frac{1}{3}\oint_{S_b^{(l)}} \boldsymbol{r}\cdot\boldsymbol{n}\,\mathrm{d}s, \tag{2.8}$$

$$\boldsymbol{r}_b^{(l)} = \frac{1}{Vol_b^{(l)}}\int_{Vol_b^{(l)}} \boldsymbol{r}\,\mathrm{d}V = \frac{1}{2Vol_b^{(l)}}\int_{Vol_b^{(l)}} \nabla(\boldsymbol{r}\cdot\boldsymbol{r})\,\mathrm{d}V = \frac{1}{2Vol_b^{(l)}}\oint_{S_b^{(l)}} (\boldsymbol{r}\cdot\boldsymbol{r})\boldsymbol{n}\,\mathrm{d}s. \tag{2.9}$$

The velocity of the centroid of bubble l can be obtained in the same way:

$$\boldsymbol{V}_b^{(l)} = \frac{1}{Vol_b^{(l)}}\int_{Vol_b^{(l)}} \boldsymbol{v}\,\mathrm{d}V = \frac{1}{Vol_b^{(l)}}\int_{Vol_b^{(l)}} \nabla\cdot(\boldsymbol{r}\boldsymbol{v})\,\mathrm{d}V = \frac{1}{Vol_b^{(l)}}\oint_{S_b^{(l)}} \boldsymbol{r}(\boldsymbol{v}\cdot\boldsymbol{n})\,\mathrm{d}s, \tag{2.10}$$

or by differentiating the path of the centroid

$$\boldsymbol{V}_b^{(l)} = \frac{\mathrm{d}\boldsymbol{r}_b^{(l)}}{\mathrm{d}t}. \tag{2.11}$$

It has been verified numerically that these two formulae give identical results. The latter formula is used in this paper.

In order to be compatible with the formulation introduced by Ishii, Chawla &

Zuber (1976) for drift-flux models, the rise velocities are presented as drift velocities. The drift velocity of bubble l, $\boldsymbol{V}_d^{(l)}$, is defined as the volume-averaged velocity of the bubble, $\boldsymbol{V}_b^{(l)}$, minus the volume-averaged velocity of the whole mixture, $\alpha \boldsymbol{V}_b + (1-\alpha)\boldsymbol{V}_f$. The average drift velocity is therefore simply

$$\boldsymbol{V}_d = (1-\alpha)\boldsymbol{V}_r. \tag{2.12}$$

The drift velocity and the relative velocity are approximately equal in dilute flows. Note that the $\rho_0 \boldsymbol{g}$ term in the Navier–Stokes equation, equation (2.2), imposes that the mass-averaged velocity, $\boldsymbol{V}_m = (\alpha\rho_b \boldsymbol{V}_b + (1-\alpha)\rho_f \boldsymbol{V}_f)/(\alpha\rho_b + (1-\alpha)\rho_f)$, is zero at all times.

Two-phase models of bubbly flows generally employ ensemble-averaging to define average quantities (Delhaye 1974; Ishii 1975; Drew 1983). Because of the computational cost of our simulations, it was not possible to do several runs with different initial configurations for each set of the governing parameters. Instead, the ensemble averages are replaced with space and time averages. In this paper, the velocity is averaged first over all bubbles,

$$\boldsymbol{V}_b(t) = \frac{1}{N_b} \sum_{l=1}^{N_b} \boldsymbol{V}_b^{(l)}(t), \tag{2.13}$$

and then over time to obtain the mean component of the bubble velocity:

$$\boldsymbol{V}_b = \frac{1}{T} \int_T \boldsymbol{V}_b(t)\, \mathrm{d}t. \tag{2.14}$$

The fluctuating component of the bubble velocity is defined as follows. The instantaneous bubble velocity variance, sometimes called suspension temperature (Nott & Brady 1994; Spelt & Sangani 1998), is calculated with respect to the instantaneous average bubble velocity $\boldsymbol{V}_b(t)$. The fluctuation velocity at each instant is the square root of the variance:

$$V'_{b_i}(t) = \sqrt{\frac{1}{N_b} \sum_{l=1,N_b} \left(V_{b_i}^{(l)}(t) - V_{b_i}(t)\right)^2}, \tag{2.15}$$

where $i = 1, 2, 3$. Note that V'_{b_i} is defined with respect to the rise velocity or relative velocity, and not the drift velocity. The mean fluctuation velocity is defined as the square root of the average variance over time:

$$V'_{b_i} = \sqrt{\frac{1}{T} \int_T V'_{b_i}(t)^2\, \mathrm{d}t}. \tag{2.16}$$

An alternative procedure is to define the fluctuations with respect to the time-averaged velocity:

$$V'_{b_i} = \sqrt{\frac{1}{N_b} \sum_{l=1,N_b} \frac{1}{T} \int_T \left(V_{b_i}^{(l)}(t) - V_{b_i}\right)^2 \mathrm{d}t}. \tag{2.17}$$

The first averaging procedure is used here because it is a better measure of the relative motion of the bubbles than the second one. Consider a situation where all bubbles move together for a short period of time without motion relative to each other. Their fluctuation velocity in this period of time is zero if equations (2.15) is used, but non-zero if equation (2.17) is used. Nott & Brady (1994) made the

same choice in the definition of the variance of a suspension of solid particles in a pressure-driven flow. Esmaeeli & Tryggvason (1996) conducted several simulations of two-dimensional bubbly flows using the same governing parameters but different initial bubble distributions. After the initial transient, all systems reached the same statistical steady state. We checked that using equations (2.15) and (2.16) rather than equation (2.17) leads to a relative difference of less than 1% in all our simulations with 27 or more bubbles and equal to about 3% for the simulations with 12 or 13 bubbles. For even smaller systems, the error is larger, but the small size of these systems precludes any accurate estimation of the variance anyway.

The fluctuation velocities of the bubbles are different from the Reynolds stress of the fluid inside the bubbles. While the fluctuation velocities of the bubbles have a strong influence on the motion of the continuous phase, recirculation of the fluid inside the bubbles is of much smaller importance since the density of the bubbles is small.

The bubble velocities are presented as Reynolds numbers and are normalized by the diameter d of the bubbles and the viscosity μ_f and density ρ_f of the outer fluid. The Weber number is defined as $We = \rho_f W_b^2 d/\sigma$. The lengths are normalized by the bubble diameter d. Similarly, the turbulence properties of the liquid phase are normalized by d and g. These quantities are also estimated by spatial and temporal averaging. For example, the spatial average of the Reynolds stress is defined as

$$\langle u_i' u_j' \rangle(t) = \frac{1}{\Omega_f} \int_{\Omega_f} u_i' u_j' \, \mathrm{d}V, \tag{2.18}$$

where Ω_f is the volume occupied by the liquid in the periodic cell and u_i' is the fluctuating component of the liquid velocity. The mean or time-averaged Reynolds stress is

$$\langle u_i' u_j' \rangle = \frac{1}{T} \int_T \langle u_i' u_j' \rangle(t) \, \mathrm{d}t. \tag{2.19}$$

2.4. *Resolution tests*

A number of validation tests of the method are reported in Tryggvason *et al.* (2001), Esmaeeli & Tryggvason (1998), and Jan (1994). For example, Jan (1994) implemented the method in axisymmetric coordinates and compared the results for the rise of a single bubble at $Re = 20$ and $We = 12$ with those of Ryskin & Leal (1984). Using a large domain and about 25 grid points per bubble radius, Jan (1994) found that the difference in the steady-state rise velocities was less than 1%, and that the bubble shape, streamlines and recirculation behind the bubble were almost identical.

Our goal is to study the motion and interaction of systems containing a number N_b of bubbles. The results of Esmaeeli & Tryggvason (1999) and the results presented in this paper indicate that the fluctuation velocity of the bubbles and the Reynolds stress in the liquid phase depend strongly on N_b. It is therefore desirable to simulate systems with large numbers of bubbles to obtain results that are independent of the size of the periodic cell. However, the high cost of three-dimensional computations imposes a limit on the resolution that can be used for each individual bubble. The resolution requirements increase with Reynolds number and void fraction α and are expressed in terms of the number of grid points per bubble diameter, n_d. Resolutions between 20 and 25 grid points per bubble diameter were used in the present simulations, depending on the void fraction. Three three-dimensional grid-independence studies were conducted for $\alpha = 6\%, 12\%$ and 24% to show that these resolutions are adequate for nearly spherical bubbles at Galileo number $N = 900$. In each case, the rise of

α (%)	n_x	n_d	Re_d	k/gd (10^{-2})
6	22	10.7	26.18	4.261
	42	20.4	30.38	4.669
	80	38.9	31.74	4.749
12	18	11.0	19.64	4.253
	34	20.8	22.82	4.775
	68	41.6	23.45	4.875
24	24	18.5	14.12	4.093
	32	24.7	15.24	4.446
	64	49.3	15.91	4.666

TABLE 1. Resolution tests for one bubble in a regular array in a cubic domain. As the number of grid points in the computational domain, $n_x = n_y = n_z$, is increased, the number of grid points per bubble diameter, n_d, increases in proportion. Tests were performed for three resolutions for each value of α: coarse, intermediate and fine. The results show that the relative error between the intermediate and fine resolution is at most 4.4% for the steady-state drift Reynolds number of the bubble, Re_d, and 4.7% for the steady-state turbulent kinetic energy of the liquid phase, k.

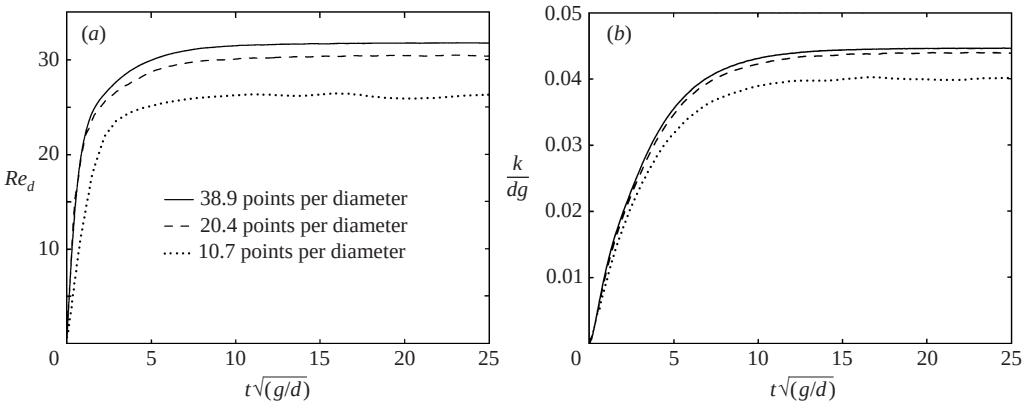

FIGURE 1. Resolution test for a regular array with $Eo = 1$, $N = 900$, $\alpha = 6\%$. (*a*) Drift velocity; (*b*) turbulent kinetic energy in the continuous phase.

a single bubble in a periodic cell was simulated on three increasingly refined grids. The rise velocity is shown in figure 1 for the $\alpha = 6\%$ case. After an initial transient, the motion of the bubble quickly settles to a steady-state value, which increases monotonically with resolution. The relative difference in the average rise velocity between $n_d = 20.4$ and $n_d = 38.9$ is 4.3% and the difference in the relaxation time, $\tau = \int_0^\infty (1 - W_d(t)/W_d)\,\mathrm{d}t$ is 3.3%. The steady-state values of the rise velocity and the continuous-phase turbulent kinetic energy are reported in table 1. For both quantities and all values of void fraction, the relative error between the intermediate and high resolution cases is less than 4.5%. The simulations reported in the results section use resolutions corresponding to the intermediate case. Because of its prohibitive cost, no resolution study was done for $\alpha = 2\%$, but the trend shown in the tests at higher values of α suggests that the value of n_d used in the results section, $n_d = 21.6$, leads to errors that are smaller than the errors at $\alpha = 6\%$.

These three-dimensional simulations showed that the differences between resolutions of about 20 and about 40 points per diameter are small. Since it is practically

n_x	n_d	Re_d	k/gd
64	19.5	25.27	0.681
128	39.1	26.30	0.670
256	78.1	26.34	0.668

TABLE 2. Resolution test for one bubble in a regular array in a two-dimensional square domain with resolution $n_x = n_y$ and n_d grid points per bubble diameter. The data show that a resolution of $n_d \approx 40$ provides grid-independent values of the steady-state drift Reynolds number Re_d and steady-state turbulent kinetic energy k. Note that k in two dimensions is one order of magnitude larger than k in three dimensions.

n_x	n_d	Re_d	Re'_b	k/gd
128	19.5	13.65	10.063	1.192
256	39.1	14.32	10.166	1.123

TABLE 3. Resolution test for a free array with nine bubbles in a two-dimensional square domain with resolution $n_x = n_y$ and n_d grid points per bubble diameter.

impossible to increase resolution further in three dimensions, a grid-independence study was conducted in two dimensions with resolutions of about 20, 40 and 80 points per diameter. Although the resolution requirements in two and three dimensions are not exactly identical, this study gives us additional confidence that the numerical resolutions used in the three-dimensional simulations reported in the paper are adequate. The two-dimensional code uses the same method as the three-dimensional code. The rise of a single bubble in a periodic domain was simulated at $N = 900$, $Eo = 0.28$, and $\alpha = 7.4\%$. Because two-dimensional bubbles deform more than their three-dimensional counterparts, a lower value of the Eötvös number was selected so that the bubble remains approximately cylindrical. The results in table 2 show that a resolution of about 40 points per bubble diameter provides a solution that is grid independent.

In addition to the rise velocity of the bubbles and the turbulence properties of the liquid phase, we are interested in determining the fluctuations of the bubble motion and must therefore verify that the interaction of multiple bubbles is correctly accounted for by the numerical method. We performed another two-dimensional grid independence study with nine bubbles at $N = 900$, $Eo = 0.28$, and $\alpha = 16.5\%$, again as a substitute for a much more expensive three-dimensional study. The simulations were conducted over a long period of time so that the time averages are well defined. In addition to the average drift velocity and the turbulent kinetic energy in the liquid phase, the total fluctuation Reynolds number, defined as the square root of the variance of the bubble velocities, $Re'_b = (Re'^2_{b_x} + Re'^2_{b_y})^{1/2}$, is reported in table 3. The relative differences of the values on the two grids are respectively 4.8%, 0.7% and 5.8% for the drift velocity, fluctuation velocity, and turbulent kinetic energy. Note that Re'_b is of the same order of magnitude as Re_d, which is characteristic of two-dimensional simulations of free arrays in this range of parameters, where the interactions between bubbles are much stronger than in three dimensions (Esmaeeli & Tryggvason 1999). These results indicate that the error in the velocity fluctuations due to finite grid discretization will be small. Note, however, that the uncertainty due to statistical variability may be large when the number of bubbles and the simulation time are small, as shown in Part 2.

2.5. *Rise velocity of a single bubble*

The rise velocity of a single bubble in an unbounded flow serves as a reference in the limit when the void fraction tends to zero. Because the numerical code uses a uniform grid and periodic boundary conditions, it is very expensive to calculate the motion of a bubble in an unbounded flow. Instead, an approximate value of the rise velocity is determined in this section from the numerical and experimental data available in the literature. The drag coefficient is defined by $C_D = 8D/\frac{1}{2}\rho_f W_T{}^2\pi d^2$, where $D = \frac{1}{6}\pi d^3(\rho_f - \rho_b)g$ is the drag and W_T is the terminal velocity. C_D is formally related to the Eötvös, Morton and Galileo numbers by $C_D = 4Eo^{3/2}/3Re^2M^{1/2} = 4N/3Re^2$. Although a considerable amount of literature exists on the rise velocity of a bubble (Clift *et al.* 1978; Bhaga & Weber 1981; Ryskin & Leal 1984; Fan & Tschuyia 1990; Duineveld 1995; Maxworthy *et al.* 1996; McLaughlin 1996), very little of it is relevant to the situation of a contamination-free bubble that is slightly deformed with $Eo = 1$ and $N = 900$. Most experiments have been performed in water and are strongly affected by surface-active agents, especially for small spherical bubbles.

Ryskin & Leal (1984) simulated the rise of a single bubble using a boundary-fitted finite difference mesh. The data of figure 1 of their paper is interpolated to determine Re. For $We \approx 1$, they report $C_D \approx 1.43$ for $Re = 20$ and $C_D \approx 0.71$ for $Re = 50$. By using a function of the form $C_D = (A/Re)(1 + (B/Re^{1/2}))$ and estimating the error arising when reading the data from the figure, the rise Reynolds number is $Re = 36.0 \pm 1.5$. A second, less accurate method to evaluate Re is to use a correlation for contaminated drops and bubbles (Clift *et al.* 1978, pp. 176–178) to find $Re \approx 25.5$, and to multiply this value by a correcting factor for a pure system. For $Eo = 1$, this factor is approximately 1.35, so that $Re \approx 34.5$.

More data are available for bubbles that are exactly spherical, but they also exhibit a considerable degree of scatter. Interpolating Ryskin & Leal's data at $We = 0$ gives $Re = 40.0 \pm 1.5$. A fit of numerical predictions of drag on spherical bubbles (Clift *et al.* 1978, p. 130), $C_D = 14.9Re^{-0.78}$, gives $Re = 36.5$. Yuan & Prosperetti (1994) simulated the rise of two bubbles in line by a method similar to Ryskin & Leal's. When the distance between the two bubbles is very large, the drag coefficient of the leading bubble can be used to estimate the drag coefficient of a single bubble in an unbounded flow, which results in $Re = 38 \pm 1.5$.

A Galileo number $N = 900$ corresponds to an air bubble with a 0.452 mm diameter in water. Katz & Meneveau (1996) measured the terminal velocity of air bubbles in purified water. For 0.475 mm diameter bubbles, they obtained $Re = 35$. Duineveld (1995) performed experiments in hyperdistilled water, but did not report results for bubbles that are as small. For contamined bubbles, Clift *et al.* (1978, p. 172) give $Re \approx 20.7$ and Nguyen (1998) gives $Re \approx 21.8$ (the properties of water are taken at room temperature). As can be expected, this value agrees well with that obtained for a rigid sphere using a correlation for the standard drag curve (Clift *et al.* 1978, p. 112), which is $Re = 21.4$.

Since comparisons will be made with results from studies in the Stokes flow and potential flow limits, the values obtained by using the drag laws in these limits are also given here for completeness in the case of a spherical bubble at $N = 900$. In Stokes flow, $C_D = 16/Re$, which leads to $Re = 75.0$ for $N = 900$. In potential flow, $C_D = 48/Re$, so that $Re = 25.0$.

To summarize, the rise Reynolds number that is taken as a reference for the case of a single bubble rising steadily in an unbounded flow with $Eo = 1$ and $N = 900$ is that derived from Ryskin & Leal's paper, $Re = 36.0$, corresponding to $C_D = 0.93$. For

a spherical bubble ($Eo = 0$) with $N = 900$, we take the average value of the three results cited above, $Re = 38.0$. Even if the scatter of the different sources is accounted for, it seems that the finite Eötvös number has a small but noticeable effect on the rise velocity. Therefore, we expect the quantitative results presented in this paper to differ slightly from these that would be found for bubbles that are exactly spherical. This is discussed further below.

2.6. *Effect of the surface tension*

A 0.452 mm diameter air bubble in water has an Eötvös number of 0.0275 and is spherical. Small values of Eo lead to large numerical errors in the discretization of the surface tension, characterized by the appearance of spurious currents. This problem is not unique to the front-tracking method, it appears also in the volume-of-fluid and level-set methods (Lafaurie *et al.* 1994). A simulation with Eötvös number $Eo = 0.1$ and $N = 900$ was performed for a regular array with $\alpha = 6\%$ on a 64^3 grid. The results were compared with the corresponding results for $Eo = 1$ in order to assess the effect of surface tension and finite deformation. At steady state, the ratios of the lengths of the major axis and minor axis of the bubble is 1.08 for $Eo = 1$ and 1.006 for $Eo = 0.1$. The relative differences of the steady-state values of the rise velocity and the turbulent kinetic energy of the liquid phase are 0.7% and 1.0% respectively. These differences are sufficiently small that the results of this paper are expected to be relevant to spherical bubbles. The case of more deformable bubbles is discussed in Bunner & Tryggvason (2002*b*), where fundamental differences are observed between $Eo = 1$ and $Eo = 5$.

2.7. *Effect of the density and viscosity ratios*

The ratios of the densities and viscosities of the bubbles and the suspending fluid are typically very small in most bubbly flows of interest. For example, for air bubbles in water at room temperature, $\rho_b/\rho_f = 1.22 \times 10^{-3}$ and $\mu_b/\mu_f = 1.81 \times 10^{-2}$. However, the multigrid solver used here fails to converge in the solution of equation (2.6) for the pressure if the density ratio is very small. An SOR solver is more robust, but its use is impractical because it increases the computational time required to achieve the same accuracy by one to two orders of magnitude. Similar problems of increased computational cost are encountered in boundary integral methods when the viscosity ratio is different from one (Pozrikidis 1993; Loewenberg & Hinch 1996). We elected to increase ρ_b and μ_b, so that $\rho_b/\rho_f = \mu_b/\mu_f = 1/50$ in all simulations presented in the results section. If the values of the density and the viscosity of the bubbles are very small compared to the values of the surrounding fluid, the pressure and viscous forces exerted by the gaseous medium inside the bubble on the interface are small. Indeed, analytical solutions in the Stokes flow limit (Clift *et al.* 1978, p. 33) show that if the viscosity of the bubble is one fiftieth the viscosity of the outer fluid, the rise velocity is reduced by only 1.0% compared to the rise velocity of a bubble with zero viscosity. Likewise, the added mass coefficient of a bubble whose density is one fiftieth the density of the outer fluid is smaller than the added mass coefficient of a bubble with zero density by 5.8% (Clift *et al.* 1978, p. 304). Numerical tests with our method by Jan (1994) showed that ratios of 1/40 and 1/400 resulted in rise velocities that differed by about 1.0%. The results of simulations with $\rho_b/\rho_f = \mu_b/\mu_f = 1/50$ should therefore apply to situations where the density and viscosity ratios are much lower. Oka & Ishii (1999) arrived at the same conclusion in their numerical simulations of gas bubbles using the level-set method.

$\alpha(\%)$	N_b	L/d	n_x	n_d	$T_f\sqrt{g/d}$	$T_i\sqrt{g/d}$	z_b/d	z_b/L	*nstep*	CPU	*procs*
2	27	8.91	192	21.6	245	60	217	24.4	60720	80	8
3	13	6.10	128	21.0	126	35	109	17.8	25590	34	8
6	2	2.59	52	20.0	68	35	63	24.4	14510	—	1
6	4	3.27	64	19.6	57	35	48	14.6	11710	—	1
6	12	4.71	92	19.5	104	30	80	17.1	21250	50	4
6	27	6.18	128	20.7	257	30	183	28.7	58990	79	8
6	91	9.26	192	20.7	142	30	109	11.7	32430	54	8
6	216	12.35	256	20.7	142	30	109	8.8	32880	126	8
12	27	4.90	104	21.2	200	30	119	24.2	47710	78	8
12	54	6.18	128	20.7	111	40	74	12.0	29050	46	8
24	27	3.89	96	24.7	228	100	104	26.7	75030	88	8

TABLE 4. List of the free array simulations, the computational parameters, and the timings. $n_x = n_y = n_z$ is the number of grid points in each spatial direction. n_d is the number of grid points per bubble diameter. T_f is the time at which the simulation was stopped. $[T_i, T_f]$ is the time interval on which the mean values are calculated; T_i is chosen in such a way that the initial transients are avoided. z_b is the average distance travelled by the bubbles in the vertical direction. *nstep* is the number of time steps. CPU is the run time in days. *procs* is the number of processors.

3. Results

All simulations reported in this paper are for a triply periodic cubic cell with $Eo = 1$ and $N = 900$ ($M = 1.2345 \times 10^{-6}$). Both regular and free arrays are considered. Regular arrays correspond to the special case where there is only one bubble in the periodic cell, so that all bubbles in the flow deform in the same way, move with the same velocity, and have a fixed and constant distance from their neighbours. Free arrays, with two or more bubbles per period, provide additional degrees of freedom and a more realistic approximation to homogeneous flows by allowing for relative motion between the bubbles. It is computationally less expensive to simulate regular arrays than free arrays, and regular arrays are sometimes used as a first approximation to homogeneous flows (Saffman 1973). However, it is known that the results for regular arrays differ in many aspects from those for irregular arrays. For example, in the sedimentation of solid particles in Stokes flows at low volume fraction α, the sedimentation velocity in a random free array is $W_d(\alpha) = W_T(1-6.55\alpha)$, where W_T is the velocity of a single particle in an unbounded flow, whereas it is $W_d(\alpha) = W_T(1 - 1.76\alpha^{1/3})$ for a regular array in a cubic lattice (Saffman 1973). Our results show that the differences between free and regular arrays are strong at low volume fraction and decrease when the volume fraction becomes large.

The effect of system size is studied by varying the number of bubbles N_b from 1 to 216. This is achieved by keeping all dimensional parameters constant and increasing the size of the periodic cell. The effect of void fraction is studied for regular arrays ($N_b = 1$) and α varying from 0.75% to 24% and for free arrays with N_b equal to 13, 27 and 54 and α varying from 2% to 24%. It is shown that a system with 12 bubbles gives a good estimate of the average bubble velocity. However, it will be shown in Part 2 that the bubble and liquid fluctuation velocities depend strongly on the system size.

Table 4 contains a list of the simulations of free arrays, along with the main computational parameters and timings of each simulation. The total CPU time is the run time multiplied by the number of processors. Most of the simulations of free arrays were performed on eight nodes of two IBM SP2 at the University of Michigan's

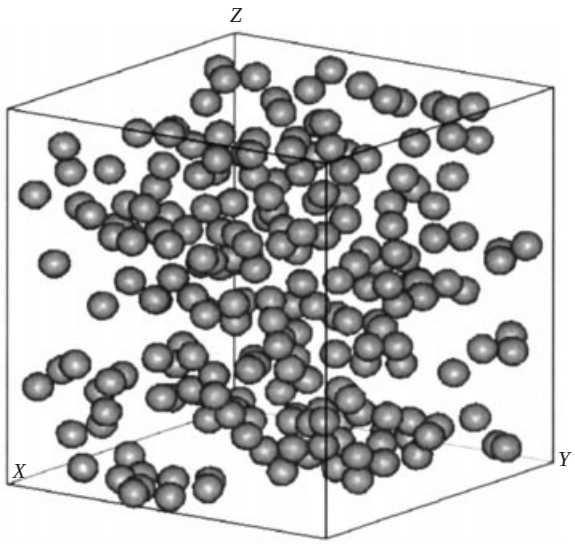

FIGURE 2. The 216 bubbles at $t = 141$.

Center for Parallel Computing and at the Maui High Performance Computing Center. These computers have P2SC processors running at a clockspeed of 160 MHz and are capable of a peak performance of 640 MFlops each. For the largest run, with 216 bubbles on a 256^3 grid, the total memory requirement was 3.76 gigabytes. The simulations with four bubbles or less were done on workstations and were not timed.

The initial location of the bubbles in the free arrays is determined in the following manner. The bubbles are first arranged in a regular array, where the distances between the centres of neighbouring bubbles are identical and equal to $\Delta_x + d$, $\Delta_y + d$, and $\Delta_z + d$ in the x-, y- and z-directions respectively, where Δ_x, Δ_y and Δ_z are the grid steps in the three spatial directions and d is the bubble diameter. For each bubble, Δ_x, Δ_y and Δ_z are then multiplied by three random numbers drawn from a uniform distribution in the $[-0.5, 0.5]$ interval, and the bubble is displaced by the resulting amounts in the x-, y- and z-directions. The initial location of the bubbles can thus be described as a perturbed regular array. We are interested in determining the average motion of the bubbles and it will be shown that the average results beyond the initial transient phase of the rise motion do not depend on the initial position of the bubbles. While the exact manner in which the array is perturbed is not important, it is critical that the array be somewhat perturbed. A two-dimensional calculation with nine bubbles initially in a perfect regular array showed that the array breaks up due to accumulation of small numerical roundoff errors, but only after the bubbles moved by a distance of about 40 bubble diameters. The initialization procedure described above could not be used for the simulations with 2, 4, 13 and 91 bubbles. Instead, we determined the initial positions of the bubbles in an *ad hoc* fashion.

3.1. *Flow visualization*

Figure 2 shows the 216 bubbles at non-dimensional time $t = 141$. The boundaries of the computational domain are marked by black lines. At this time, the bubbles have risen by an average distance of 109 bubble diameters or 8.8 periodic boxes. Although the bubbles form transient clusters, movies of the simulation results show that they are on average distributed uniformly throughout the computational domain. The

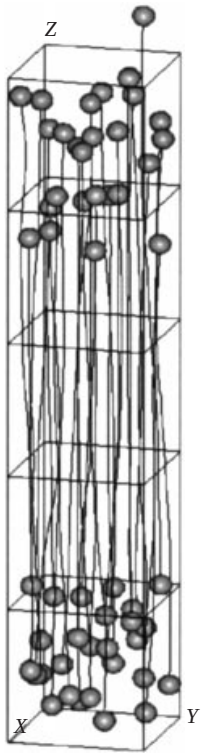

FIGURE 3. Position of the 27 bubbles at $\alpha = 6\%$ at $t = 14$ and $t = 43$ and the paths of the centroids of the bubbles.

trajectories of the 27 bubbles for $\alpha = 6\%$ are plotted in figure 3 between $t = 14$ and 43. The 27 bubbles are initially located within one periodic box. As the bubbles rise and disperse, they move into the neighbouring periodic boxes. The unsteadiness of the flow is visible in the paths of the centroids of the bubbles. Since a single bubble in an infinite domain at $Eo = 1$ and $N = 900$ rises steadily, this unsteadiness is clearly due to the interaction of each bubble with its neighbours. The rise velocities of the 27 bubbles are plotted versus time in figure 4. This simulation was continued until $t = 257$ (see table 4) but only the values until $t = 100$ are shown for clarity. The rise velocities of the individual bubbles do not reach steady state values, in contrast to the results of numerical simulations based on a potential flow approximation of the bubbly flow by Smereka (1993) and Sangani & Didwania (1993). These authors find that the individual rise velocities become constant and equal. This has not been seen in experiments. We believe that the discrepancy between potential flow simulations on one hand and experiments and finite Reynolds number simulations on the other hand, can be explained by the different mechanisms driving the interaction of two bubbles. This is discussed in § 3.3.

In figure 5, the 91 bubbles at $\alpha = 6\%$ are shown at $t = 63$, along with the streamlines in a vertical cross-section. The recirculation pattern around the equator of the bubbles can be seen. The strong interaction between bubbles is also clearly visible. A detail of figure 5 is shown in figure 6 and illustrates the fact that all scales of motion are resolved.

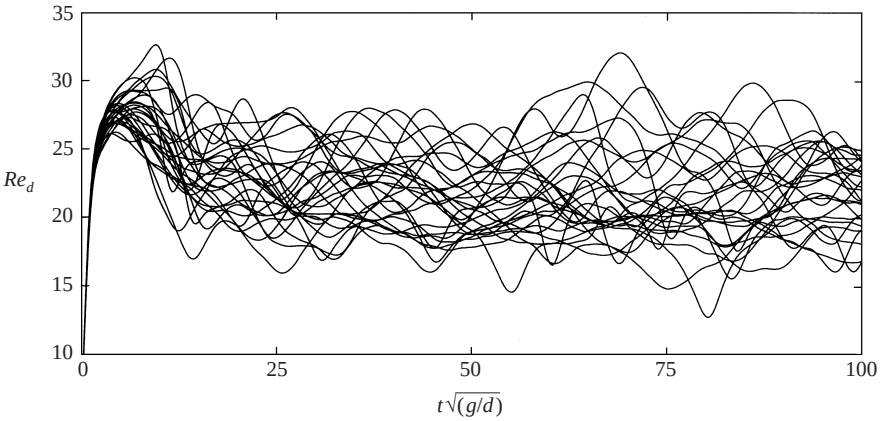

FIGURE 4. Drift velocity of the 27 bubbles at $\alpha = 6\%$ until $t = 100$.

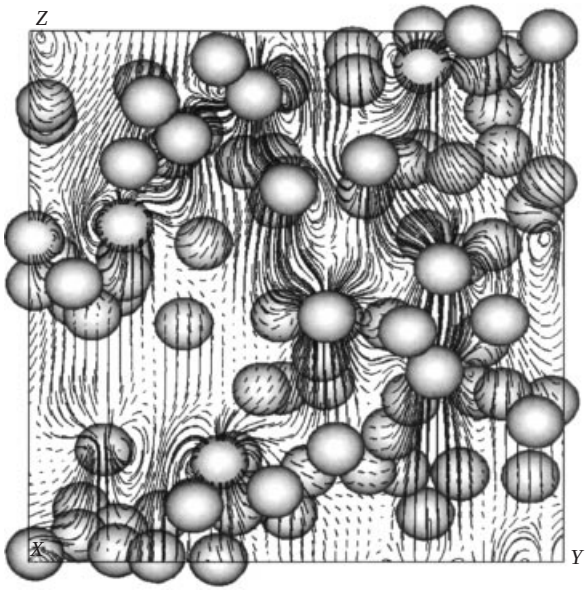

FIGURE 5. Position of the 91 bubbles at $t = 63$ and streamlines (computed by finding the pathlines at a fixed time) in a vertical cross-section.

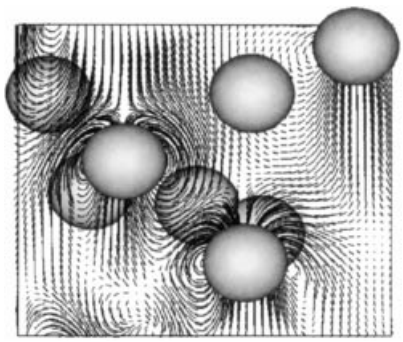

FIGURE 6. Detail of figure 5.

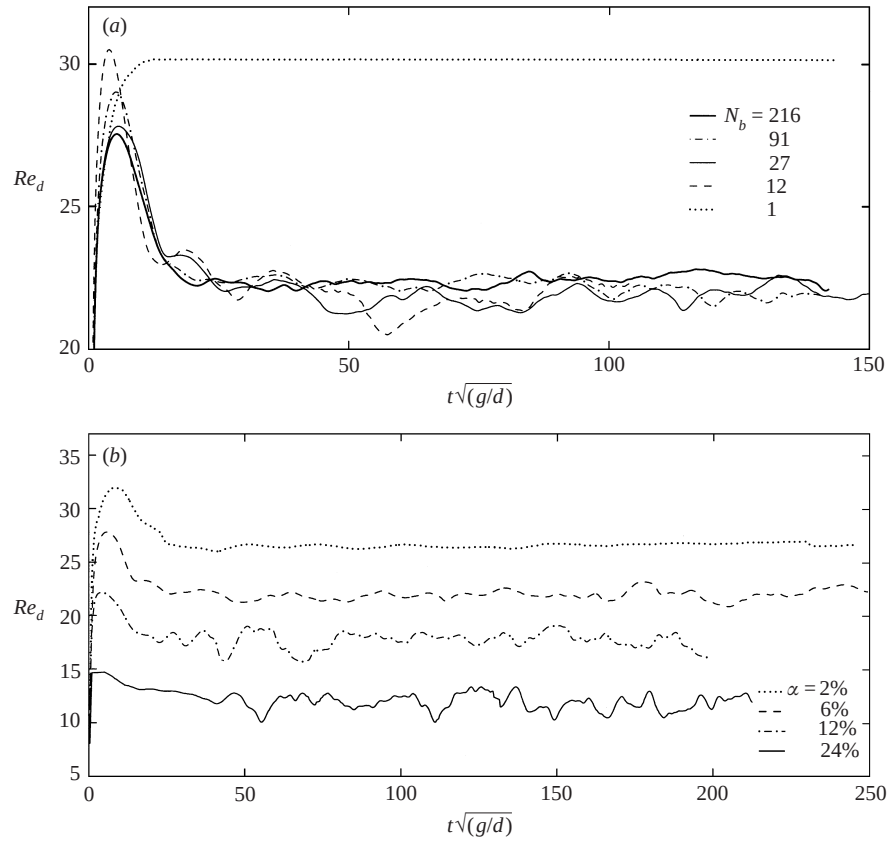

FIGURE 7. Average drift Reynolds number vs. time as a function of (*a*) system size for $\alpha = 6\%$ and (*b*) void fraction for $N_b = 27$.

3.2. *Bubble rise velocity*

The average drift Reynolds number of the bubbles, $Re_d(t)$, is shown versus time in figure 7(*a*) for the systems with $N_b = 1$, 12, 27, 91 and 216 bubbles at $\alpha = 6\%$ and in figure 7(*b*) for the systems with $N_b = 27$ and $\alpha = 2$, 6, 12 and 24%. After the bubbles are released, they undergo a short transient phase, where the bubble array retains its initial configuration and the drift velocity curves overlap approximately, as seen in figure 4. In this initial transient, the velocity of the free array approaches the steady velocity of the regular array. For $N_b = 12$, $Re_d(t)$ even exceeds the steady velocity of the regular array because the regular array was not perturbed sufficiently in the *ad hoc* initialization procedure. However, a regular array is an unstable configuration and breaks up due to interactions between the bubbles. After the initial transient peak, $Re_d(t)$ reaches a well-defined statistical steady state, even though the individual bubble velocities fluctuate throughout the simulation. The mean values in this steady state are always lower for the free arrays than for the corresponding regular arrays. Esmaeeli & Tryggvson (1999) suggested that this is due to increased deposition of vorticity due to the unsteady bubble motion and the irregular bubble distribution. This is consistent with the results of Koch & Ladd (1997), who found that irregularly positioned, fixed, circular cylinders have a larger drag than a regular array of fixed cylinders. In contrast, Esmaeeli & Tryggvason (1998) found that freely evolving arrays at $Re \sim 1-2$ rise faster than regular arrays as predicted by theories based on Stokes

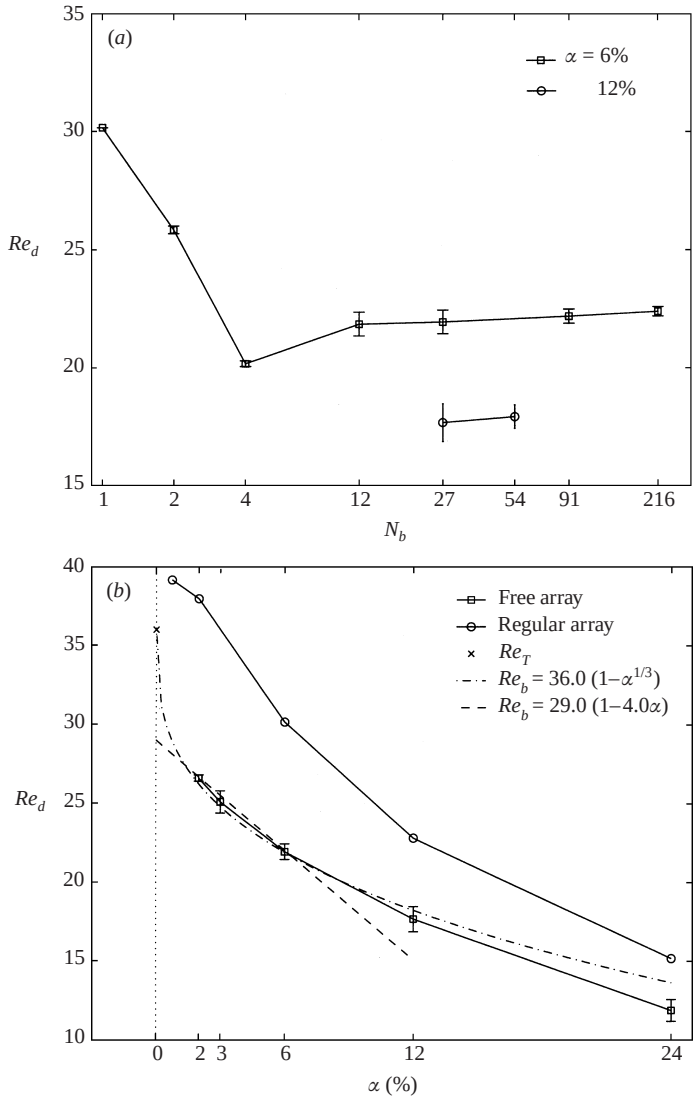

FIGURE 8. Mean drift Reynolds number as a function of (*a*) N_b for $\alpha = 6\%$ and 12% and (*b*) α for the free arrays ($N_b = 13$ and 27) and the regular arrays ($N_b = 1$). The error bars indicate the standard deviation of the data in the time interval over which it is averaged. Re_T is the terminal Reynolds number of a single bubble in an unbounded flow. $Re_b = 36(1 - \alpha^{0.3})$ provides a fit to the simulation data for the free arrays.

flow. The horizontal velocities, not shown, fluctuate around zero. The fluctuations about Re_d are high when N_b is small or α is high. The $N_b = 27$, $\alpha = 24\%$ case exhibits strong variations, which can be attributed to collective motion induced by the high packing state of this system, as discussed in § 3.3.

The effect of system size on the rise velocity is shown in figure 8(*a*). Even very small systems with two or four bubbles have markedly different rise velocities than the regular array, suggesting that such systems capture the basic dynamics of bubble interaction. However, it is necessary to simulate a larger number of bubbles to obtain more accurate results. The value of W_d increases by only 2.4% between $N_b = 12$ and

$N_b = 216$ so that the average drift velocity can be considered effectively independent of N_b when $N_b \geqslant 12$. Since the initial configurations of the bubble arrays are different in the simulations with $N_b = 12$, 27, 91 and 216 bubbles, this also indicates that the initial positions of the bubbles have no influence on the average drift velocity past the initial transient peak.

System size effects are important in simulations of sedimenting particles at low Reynolds number due to the long range of particle–particle interactions. For example, in the Stokes flow simulations of Ladd (1993), a difference of 5–10% can be seen in the sedimentation velocity when 32 and 108 particles are used at a volume fraction of 5%. At high Reynolds numbers, the velocity disturbance induced by a bubble decays much faster with distance away from the bubble than in Stokes flow. Sangani, Zhang & Prosperetti (1991) report that the average bubble velocity in their potential flow simulations changes very little for 8, 16, and 32 bubbles.

The ability to predict the dependence of the average velocity on the volume fraction is of fundamental importance in the study of dispersed multiphase flows. A brief summary of existing results for bubbles follows. van Wijngaarden (1993) determined the rise velocity of equisized spherical bubbles in dilute conditions in the case where the Reynolds number is sufficiently high that the flow can be assumed to be potential, yet the Weber number is sufficiently small that the bubbles remain spherical. From an analysis of the relative motion of a pair of bubbles, he found that the most likely orientation of the separation vector between the two bubbles is in a plane perpendicular to gravity and derived the pair probability distribution function in this plane. Using this probability density, he calculated the average rise velocity to the leading order:

$$W_d(\alpha) = W_T(1 - 1.56\alpha). \tag{3.1}$$

For comparison, he also determined the mean rise velocity by assuming that the bubbles are randomly distributed in space and randomly distributed in a horizontal plane and found, respectively,

$$W_d(\alpha) = W_T(1 - 2\alpha) \tag{3.2}$$

and

$$W_d(\alpha) = W_T(1 - 1.25\alpha). \tag{3.3}$$

The effect of the microstructure on the average rise velocity is clear. Experimental confirmation of the linear dependence of W_d on α in the high Reynolds number regime, $Re > 200$, was made for air bubbles in purified water by van Wijngaarden & Kapteyn (1990), who found

$$W_d(\alpha) = V(1 - 1.78\alpha), \tag{3.4}$$

but only for $0.02 < \alpha < 0.15$. Between $\alpha = 0$ and 2%, $W_d(\alpha)$ falls nonlinearly, V being 20% lower than the terminal rise velocity W_T. A similar sharp drop between $W_d(0)$ and $W_d(\alpha > 0)$ was observed by Zenit, Koch & Sangani (2001) in their experiments on slightly deformed bubbles at Reynolds number about 300. For $\alpha > 0$, they found:

$$W_d(\alpha) \propto (1 - \alpha)^{2.8}. \tag{3.5}$$

For the general case of particulate flows at a wide range of Reynolds numbers and deformations, Ishii & Zuber (1979) assumed a similarity criterion between the drag law of a single particle and the drag law of a multi-particle system and used a vast number of experimental data to determine $W_d(\alpha)$. For bubbles, they distinguish four regimes as the Reynolds number increases: Stokes regime, viscous regime, distorted

particle regime, and churn turbulent regime. The high Reynolds number experimental results of van Wijngaarden & Kapteyn (1990) fall into the distorted particle regime, for which Ishii & Zuber (1979) propose

$$W_d(\alpha) = W_T(1-\alpha)^{1.75}, \tag{3.6}$$

which agrees well with equation (3.4) when α is small, and also with the formula given in Hetsroni (1982, pp. 2–87). Our results are for lower Reynolds number and fall into the viscous regime, where a more complicated formula applies. However, in the range of void fraction considered here, the Ishii & Zuber (1979) correlation can be approximated by

$$W_d(\alpha) \approx W_T(1-\alpha)^{3.0}. \tag{3.7}$$

These correlations, equations (3.6) and (3.7), are derived by scaling and validated with experimental data where surface contamination plays an important role. Their direct applicability to the current results is therefore questionable, but they will serve as useful reference points. In particular, linear and power-law fits will be attempted and comparisons made with the formulae presented above.

The mean drift velocity computed from our results is shown versus α in figure 8(b); α ranges from 0.75% to 24% for the regular arrays and from 2% to 24% for the free arrays. The regular array results are discussed at the end of the section. Due to the high cost of simulating a system with a large number of bubbles at very small void fractions with our code, the lowest void fraction reported here for a free array is 2%, for which $Re_d = 26.6$. Nevertheless, as α approaches zero, $Re_d(\alpha)$ must tend towards the terminal velocity of a single bubble in an unbounded flow determined in § 2.5, $Re_T = 36.0$, implying a sharp decrease in the rise velocity from $\alpha = 0$ to $\alpha = 2\%$. Unlike the analytical results of van Wijngaarden (1993) and the experimental results of van Wijngaarden & Kapteyn (1990), which are both for much higher Reynolds numbers, $Re_d(\alpha)$ is not a linear function of α, but is slightly convex. However, if we fit lines between $\alpha = 2\%$ and 6% on one hand and between $\alpha = 2\%$ and 24% on the other hand, the slopes are in both cases higher than the slopes of equations (3.1) to (3.4), but consistent with a linearization of equation (3.7) at small α. The projections of these fits on $\alpha = 0$ give $Re_d = 28.4 \pm 0.7$ in both cases, which is about 25% lower than Re_T. The fact that $Re_d < Re_T$ and the magnitude of the difference are in agreement with the experimental results of van Wijngaarden & Kapteyn (1990) and Zenit *et al.* (2001). Zenit *et al.* (2001) attribute the sharp decrease of the mean bubble velocity at low void fractions to the collisions of the bubbles with the walls of their experimental channel. The absence of walls in our simulations shows that this factor is probably not the main reason. We believe that this nonlinear decrease is due to the change in microstructure. For $\alpha = 0$, the bubbles are distributed randomly in space and do not interact with their neighbours. For $\alpha = 2\%$, bubbles tend to align themselves horizontally relative to their neighbors, as shown in § 3.3. This change in the microstructure results in a higher drag coefficient and therefore lower rise velocity than for bubbles at $\alpha = 0$. A power law of the form of equations (3.6) and (3.7) does not provide a good fit to the computed values of $W_d(\alpha)$ and W_T, but a good fit is given by:

$$Re_d = 36.0(1-\alpha^{0.3}). \tag{3.8}$$

This expression is robust to small variations in Re_T in the simulations results, with only small changes in the exponent. It is emphasized that there is no theoretical justification for this formula.

The velocity of the regular array is greater than that of the free array for all values

of void fraction reported here. This can also be attributed to the difference in the microstructure. The regular array contains an equal number of bubble pairs aligned horizontally and vertically, whereas the free array contains a larger number of bubble pairs that are aligned horizontally. Since the drag of a horizontally aligned bubble pair is larger than the drag of a vertically aligned bubble pair, where the wake of the leading bubble shields the trailing bubble from the oncoming flow, the bubbles rise faster in the regular array than in the free array. At low void fractions, the drift Reynolds number in the regular arrays is higher than Re_T. Therefore $Re_d(\alpha)$ actually increases with α for values of α between 0 and 0.75%. The following explanation is suggested for this behavior. As mentioned previously, a bubble trailing in the wake of another bubble experiences a lower drag than an isolated bubble. In a regular array, every bubble is located in the wake of an infinite number of bubbles (its periodic images). At low void fractions, this tends to reduce the drag of the bubble and increase its rise velocity to a value larger than W_T. At high void fraction, the flow blockage due to the presence of the surrounding bubbles starts dominating over this drag reduction mechanism, so that Re_d eventually becomes smaller than Re_T.

3.3. *Microstructure*

The discussion and results above have made clear the importance of understanding the spatial distribution of the bubbles and the fundamental mechanisms which determine the interactions between them. Approximate knowledge of the microstructure or an assumption about the microstructure is necessary to determine the rise velocity analytically (van Wijngaarden 1993). Moreover, Smereka (1993) pointed out that a wrong assumption about the microstructure can lead to ill-posed models. A summary of previous studies regarding the bubble distribution is given here, starting with the interaction of two side-by-side bubbles and two in-line bubbles, moving on to multi-bubble systems in the potential flow approximation, and finishing with work at finite Reynolds numbers.

Two spheres in steady potential flow attract when they move perpendicularly to their line of centres and repel when they move in the direction parallel to their line of centres (Lamb 1932). Legendre & Magnaudet (1998) considered the motion of two spherical bubbles whose line of centres is perpendicular to the direction of motion and which are separated by a fixed distance $r = sa$, where a is the radius of the bubbles. In the potential flow limit, they report that the rise velocity is lower than the terminal velocity of an isolated bubble and that the bubbles are always attracted towards each other. The reason for this attractive force is that the pressure in the gap between the bubbles is lower than the ambient pressure. In the opposite limit of very viscous flows where the Oseen approximation is valid and small inertia effects are present, they report that the bubbles always repel and that the rise velocity is lower than the terminal velocity at short separation distances and higher at large separation distances. In the absence of inertia, the lift force is zero and the bubbles do not experience relative motion unless acted upon by a third bubble. Legendre & Magnaudet (1998) computed the motion of two side by side bubbles at $0.1 \leqslant Re \leqslant 500$ by solving the Navier–Stokes equations and confirmed the validity of the expressions derived from the Oseen approximation at low Re. They found that the lift force changes sign at $2.5 \leqslant Re \leqslant 25$ for separation distances $3 \leqslant s \leqslant 10$. However, they were unable to recover the predictions of potential flow theory, even at Re as large as 500 and attributed the discrepancy to vorticity generated at the surface of the bubble.

Harper (1970) analysed the rise of two bubbles in line at a fixed separation distance under the assumption of potential flow but with the inclusion of a thin wake between

the bubbles. He determined that the irrotational interaction results in an $O(s^{-4})$ repulsive force due to the pressure being higher in the gap between the bubbles than in the ambient flow, while the wake effect tends to move the bubbles towards each other, so that there exists an equilibrium distance at which the hydrodynamic forces balance. This equilibrium distance is stable to vertical displacements, but a vertical line of two bubbles is unstable to lateral displacements. Yuan & Prosperetti (1994) computed the in-line motion of two spherical bubbles at Re up to 200 by solving the unsteady Navier–Stokes equations. Their results agree qualitatively with Harper's (1970) theory, in particular in the existence of an equilibrium distance, but the values of the drag differ considerably, even for $Re = 200$. They also show that the transport and diffusion of vorticity affect the interaction between the bubbles very strongly. Katz & Meneveau (1996) conducted experiments of nearly spherical in-line air bubbles in purified water for $0.2 \leqslant Re \leqslant 140$. Contrary to the results of Harper's (1970) first-order boundary layer theory and Yuan & Prosperetti's (1994) Navier–Stokes simulations, they observe that the bubbles always collide and coalesce, indicating that the adverse pressure gradient is not strong enough to overcome the wake effect. Katz & Meneveau (1996) and Yuan & Prosperetti (1994) suggest that the discrepancy between the experimental and numerical results is due to bubble deformation.

The unsteady motion of a pair of spherical bubbles was studied in the potential flow approximation by Biesheuvel & van Wijngaarden (1982), Kok (1989), and van Wijngaarden (1993). When the angle θ between the line joining the bubble centres and the direction of gravity is smaller than 55° or larger than 125°, the two bubbles repel each other. When θ lies between these two values, they attract each other. The simulations and experiments of Kok (1989) show that two bubbles always approach each other along a line inclined at an angle close to $\pi/2$ and that they move towards each other until they touch. At close encounter, the bubbles bounce in singly filtrated water but coalesce in hyperfiltrated water. The first result was used by van Wijngaarden (1993), who assumed that the motion of a bubble pair is entirely in a horizontal plane in order to determine the probability density function of finding two bubbles at a given distance of each other and to calculate the average rise velocity of a dilute suspension. van Wijngaarden (1993) also showed that the second result, i.e. that the bubbles touch, leads to clustering of pairs when viscosity is present. He noted that, while the formation of horizontal bubble clusters is observed in the transition from bubbly flow to slug flow, clustering is not observed in experiments at volume concentrations well below this transition. He argued that clustering may be prevented by the effect of multiple interactions and by turbulence. However, an attempt to calculate the interaction of a third bubble with a bubble pair was inconclusive, suggesting that multiple potential interactions are not able to compensate for the tendency to cluster.

The motion of a large number of spherical bubbles in potential flow was studied numerically by Sangani & Didwania (1993), Smereka (1993), and Yurkovetsky & Brady (1996). Although the particular approaches differ, they share key features. The viscous forces are included by using Levich's expression for the drag, $\boldsymbol{F} = 12\pi\mu a\boldsymbol{V}_r$, or by differentiation of the rate of viscous energy dissipation, $\boldsymbol{F} = \frac{1}{2}\nabla\dot{E}_d$. It is assumed that colliding bubbles bounce without coalescing and that the momentum and kinetic energy of the system are conserved throughout the collision. The results of the three studies are similar. In the absence of gravity and viscous forces, when the bubbles are given initial velocities with mean in the vertical direction, they form horizontal clusters if the variance of the velocity is small, but remain randomly distributed if

the initial velocity distribution is sufficiently non-uniform. When gravity and viscous forces are included, the bubbles always aggregate in horizontal clusters. Smereka (1993) suggested that liquid turbulence may inhibit this clustering since it would increase the variance of the bubble velocities. Sangani & Didwania (1993) recognized that the assumption of an irrotational flow might be an oversimplification and that it might be necessary to include vorticity in the model, possibly as an additional random force on the bubbles. Zenit *et al.* (2001) found that some horizontal clustering occurs in experiments with bubbles at Reynolds number about 300, but not to the extent predicted by potential flow theory.

Fortes, Joseph & Lundgren (1987) examined the motion of solid spherical particles fluidized in water at high Reynolds numbers. For two spheres initially aligned vertically, they observed that the trailing particle is drafted into the wake of the leading particle. After the two particles come into contact, they rotate around each other and move away from each other while falling side by side. Fortes *et al.* (1987) called this fundamental rearrangement mechanism 'drafting, kissing, and tumbling'. They also looked at a cross-stream alignment of spheres fluidized by a water stream and noticed that the cross-stream array was a stable configuration. In fluidized beds with much larger numbers of particles at volume concentrations between 10% and 28%, they observed that these cross-stream arrays are an important feature of the flow, along with the breaking down of falling streamwise particle pairs. Direct numerical simulations of two sedimenting spheres by Feng, Hu & Joseph (1994) showed that the drafting, kissing, and tumbling mechanism accounts well for the interaction of particles at finite Reynolds numbers.

Cartellier & Rivière (2001) performed experiments with nearly spherical bubbles at $\alpha < 1\%$. They found that bubbles at $Re = O(1)$ are approximately uniformly distributed whereas bubbles at $Re = O(10)$ exhibit a preference for horizontal alignment. Esmaeeli & Tryggvason (1998, 1999) likewise found that the tendency for bubbles to line up horizontally increases with Reynolds number. In addition, Cartellier & Rivière (2001) examined the interaction of two bubbles, which are initially aligned vertically, in the case where the bubbles are clean and in the case where the bubbles are contamined. They found that contaminated bubbles experience drafting, kissing and tumbling, but that clean bubbles rarely collide, instead smoothly rotating around each other. Their results suggest that the discrepancy mentioned above between the results of Katz & Meneveau (1996) and Yuan & Prosperetti (1994) might be due to surface contamination rather than bubble deformation.

In order to understand the microstructure of bubble interactions, we examine the pair probability distribution function, $G(r, \theta)$, which is defined as the probability that the separation vector $\boldsymbol{r}_{ij}$ between the centroids of bubbles i and j has norm r and is oriented at an angle θ with respect to the direction of gravity:

$$G(r, \theta) = \frac{\Omega}{N_b(N_b - 1)} \left\langle \sum_{i=1,N_b} \sum_{\substack{j=1,N_b \\ i \neq j}} \delta(\boldsymbol{r} - \boldsymbol{r}_{ij}) \right\rangle. \tag{3.9}$$

Here Ω is the volume of the periodic cell. The configuration of bubbles i and j is illustrated in figure 9. The radial pair distribution function, $G(r)$, defined as the integral of $G(r, \theta)$ over thin spherical shells of width Δr and radius r, is shown in figure 10. The results were obtained by averaging over at least 200 evenly spaced time samples in the $[T_i, T_f]$ time intervals. Nearly identical results were obtained when Δr and the number of time samples were divided or multiplied by two. The maximum

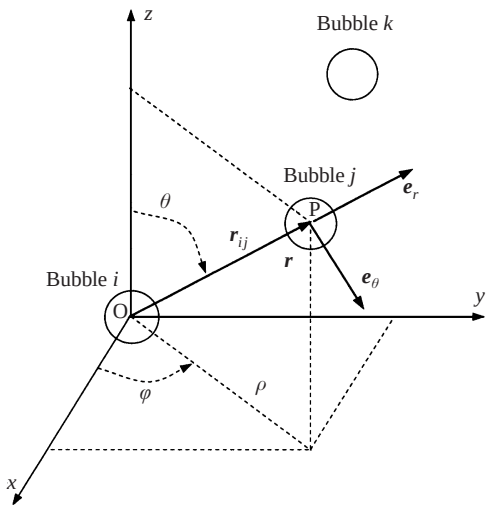

FIGURE 9. Definition of the separation vector $\boldsymbol{r}_{ij}$, distance r, and angle θ between bubbles i and j, and of the unit vectors $\boldsymbol{e}_r$ and $\boldsymbol{e}_\theta$.

values of r correspond to the size of the periodic box. Figure 10(b,c) shows $G(r)$ for $\alpha = 6\%$ and $N_b = 27$, 91 and 216. If the bubbles were spherical, $G(r)$ would be zero for $r < 2a$. Since they are slightly deformable, $G(r) > 0$ for $r > 1.8a$, indicating that collisions between bubbles do occur. $G(r)$ has a peak at $r \approx 2.8a$ and $G(r) \to 1$ as r is increased. At $\alpha = 12\%$ and 24% (figure 10d,e), the profiles of $G(r)$ are very similar, but the peaks shift to $r \approx 2.6a$ and $r \approx 2.2a$ respectively, and the values below $r = 2a$ are slightly larger. In regular arrays at $\alpha = 6\%$, 12% and 24%, the closest distances between the centroids of two bubbles are respectively $4.1a$, $3.1a$ and $2.6a$, which are larger than the distances at the peaks. Therefore, the bubbles repel each other, but not to the extent that they maximize their spacing. The more dilute case, $\alpha = 2\%$ (figure 10a), is qualitatively different in three aspects. First, $G(r) = 0$ for $r \leqslant 2.5a$, so it can be assumed that the bubbles do not come into contact in this case. This assumption was verified by calculating the minimum distance between the front points of two close bubbles (as opposed to the distance between their centroids) as a function of time. This minimum distance was found to be about $0.5a$. The second important aspect is the absence of a peak at close distance. There is a maximum, but it has lower magnitude than for $\alpha \geqslant 6\%$ and is located at a distance $r \approx 7.0a$, which is larger than the spacing of the corresponding regular array, $r = 5.9a$. The third aspect is the slow convergence of $G(r)$ as r increases.

In the Stokes flow simulations of Ladd (1997), $G(r)$ converges very slowly with r. At a volume fraction of 10%, it only reaches a constant value around $r \approx 20a$. This is due to the long range of particle interactions in Stokes flow. In our simulations, $G(r)$ converges faster and always reaches unity at a separation distance well below the size of the periodic box. This gives us confidence that the computational domain is large enough in all cases for all bubble–bubble interactions to be accounted for to a satisfying degree.

The angular pair distribution, $G(\theta)$, is shown in figure 11. $G(\theta)$ is calculated by integrating $G(r,\theta)$ over an angular sector of radius r and width $\Delta\theta$. The result is normalized so that $\int_0^\pi G(\theta)\,\mathrm{d}\theta = 1$. For r of the order of the bubble diameter, $G(\theta)$ accounts for the direct interaction of bubbles that are close. For larger values of r, it is indicative of large-scale structure formation. Like $G(r)$, $G(\theta)$ was determined by

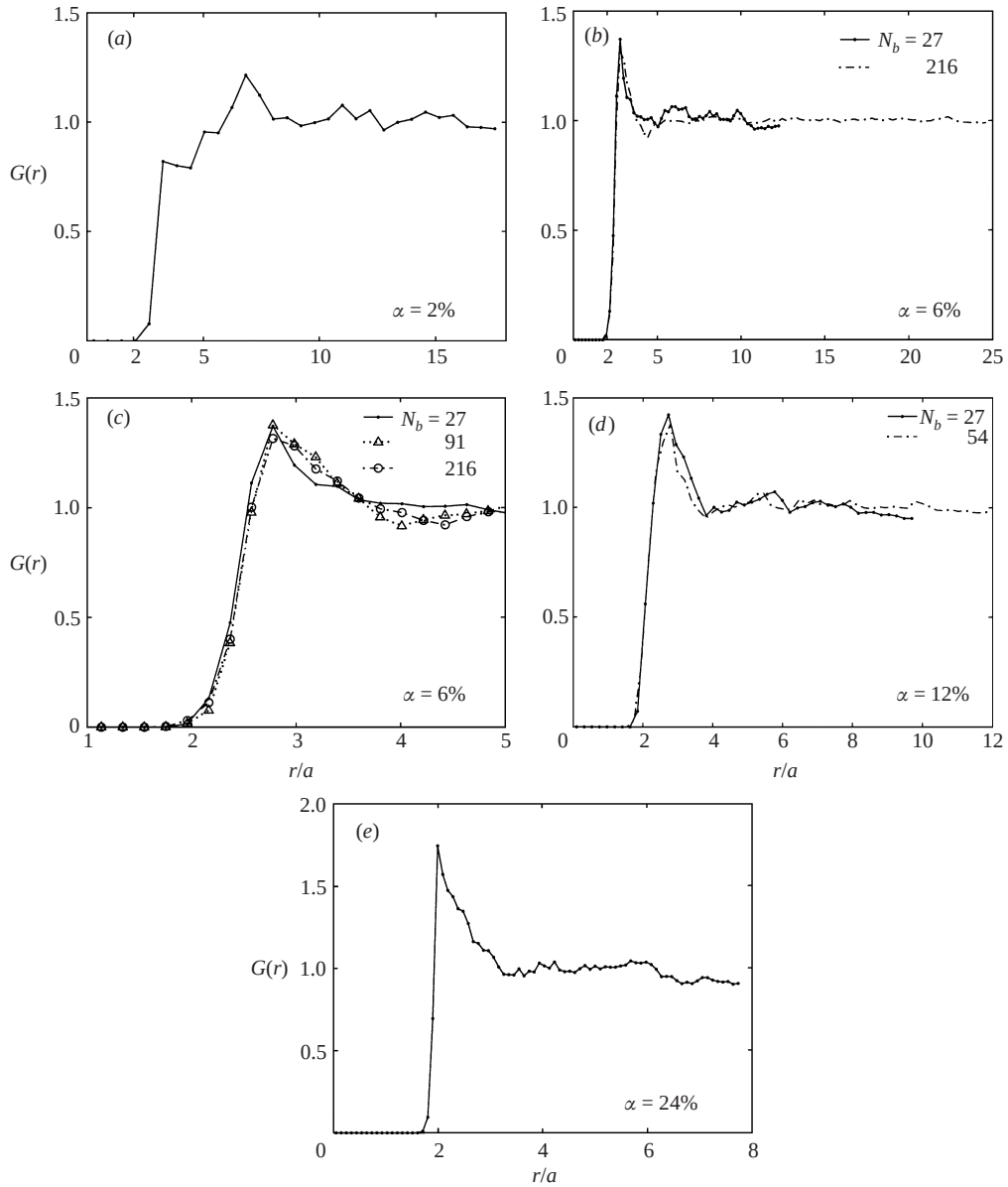

FIGURE 10. Radial pair distribution function for $\alpha = 2\%$, 6%, 12% and 24% and $N_b = 27$ for $r \in [0, L]$. The results for $N_b = 91$ and 216 are superposed in (b) and (c) and the results for $N_b = 54$ are superposed in (d).

averaging over at least 200 time samples. The $[0, \pi]$ horizontal axis is discretized into 20 intervals. A sensitivity study showed that the results do not depend significantly on the number of time samples or on the value of $\Delta\theta$, provided the number of samples is large enough and $\Delta\theta$ is not too small. If $\Delta\theta$ is chosen too small, the limited system size leads to noisy results. At small distances, all curves exhibit a peak at $\theta = \pi/2$, demonstrating a preference for pairs of bubbles to align themselves broadside to the flow, which is consistent with the findings of all previous studies cited above. For a given r, the value of $G(\pi/2)$ decreases when the void fraction increases. For example,

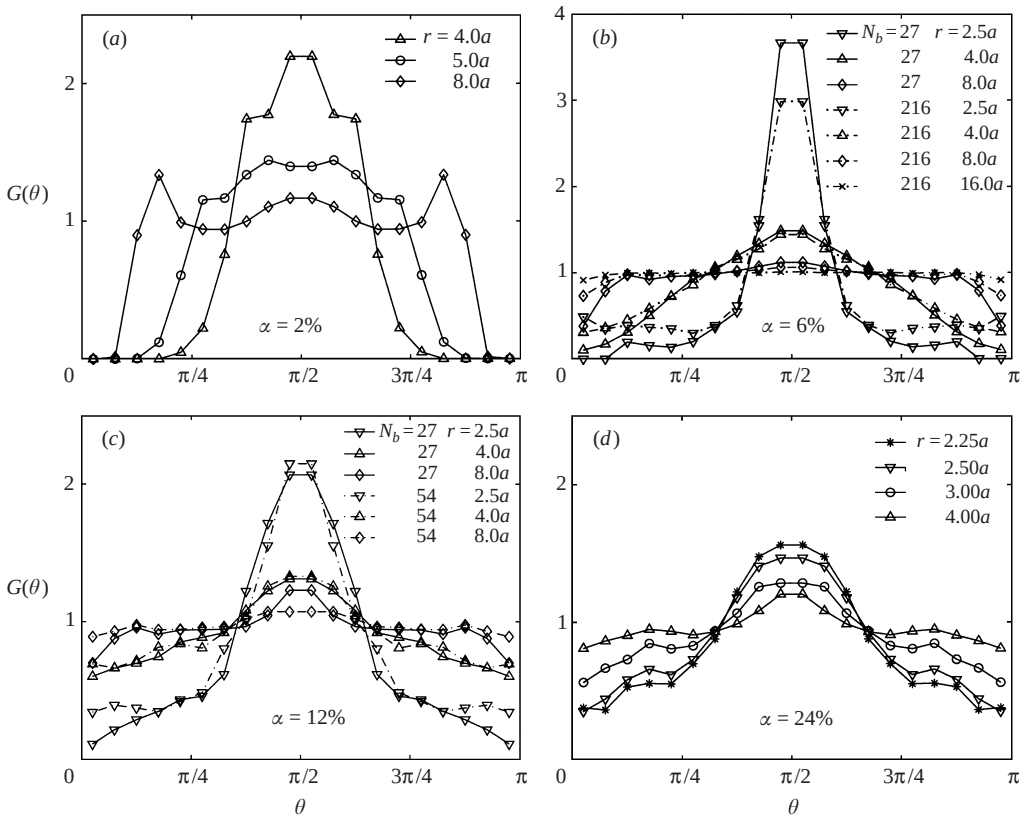

FIGURE 11. Angular pair distribution function for $\alpha = 2\%$, 6%, 12% and 24% and $N_b = 27$ and different values of the separation distance r. The results for $N_b = 216$ and $N_b = 54$ are superposed in (b) and (c) respectively.

for $r = 2.5a$, it is respectively 3.7, 2.1 and 1.5 for $\alpha = 6\%(N_b = 27)$, $12\%(N_b = 27)$, and 24%. (No sample is available at this separation distance in the $\alpha = 2\%$ case.) In addition to the peak at $\theta = \pi/2$, smaller peaks can be seen close to $\theta = 0$ and π for $N_b = 216$ at $r = 2.5a$, and for $\alpha = 2\%$ at $r = 8.0a$. This is consistent with previous studies, which show that the in-line configuration of bubbles is an equilibrium configuration too, albeit an unstable one. $G(\theta) \to 1$ when the computational domains becomes large since the bubbles are nearly uniformly distributed at large distances.

Additional understanding of the dynamics of bubble interactions can be obtained by looking at the relative velocity of bubble pairs. The polar coordinates of the centroid P of bubble j in the frame of reference defined above and illustrated in figure 9 are (r, θ), and the corresponding unit vectors are $\boldsymbol{e}_r = \boldsymbol{e}_\rho \sin\theta + \boldsymbol{e}_z \cos\theta$ and $\boldsymbol{e}_\theta = \boldsymbol{e}_\rho \cos\theta - \boldsymbol{e}_z \sin\theta$, where $\boldsymbol{e}_\rho = \boldsymbol{e}_x \cos\phi + \boldsymbol{e}_y \sin\phi$. The relative velocity of the bubble pair i, j is decomposed into its radial and tangential components along $\boldsymbol{e}_r$ and $\boldsymbol{e}_\theta$: V_r and V_θ. A simple quantitative description of the relative motion of bubble pairs can be obtained by calculating the probability of V_r and V_θ being positive as functions of θ. This is done for all bubble pairs separated by a distance less than r, in the same manner as $G(\theta)$. In a uniformly distributed suspension, $P(V_r > 0) = 0.5$ and $P(V_\theta > 0) = 0.5$.

$P(V_r > 0)$ is shown versus θ for different values of r in figure 12. The general trend is for bubble pairs to attract strongly ($V_r < 0$) when they are aligned vertically and to

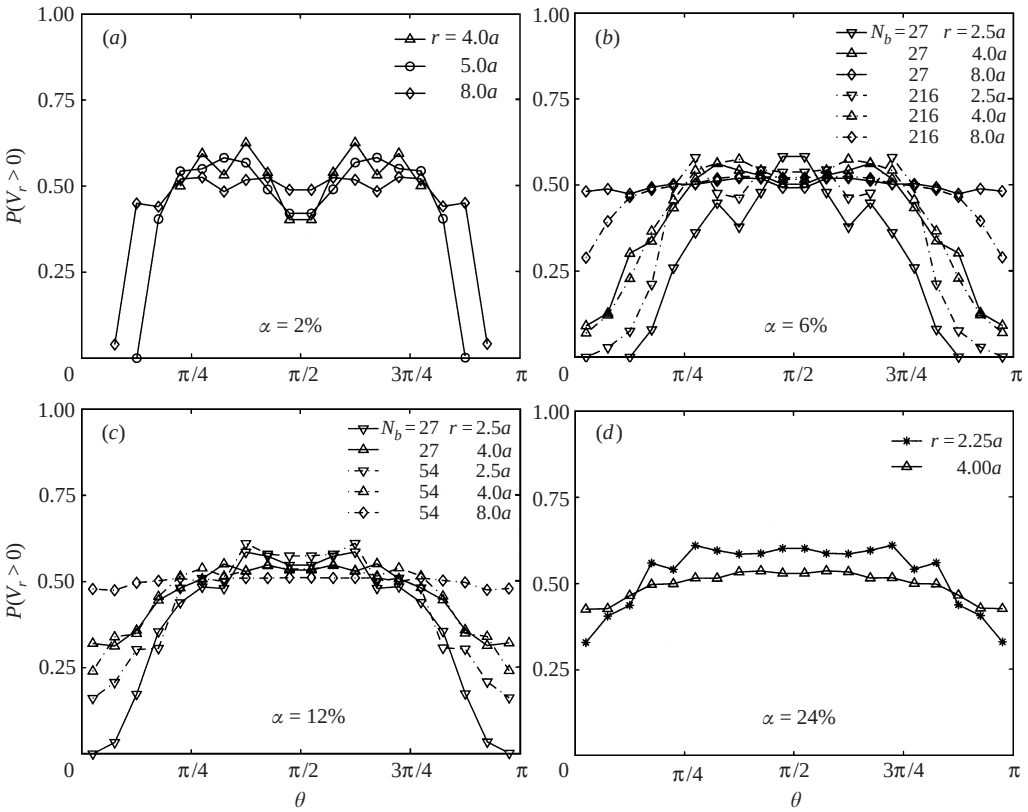

FIGURE 12. $P(V_r > 0)$, the probability that the radial relative velocity between two bubbles is positive, as a function of θ for $\alpha = 2\%$, 6%, 12% and 24% and $N_b = 27$ and different values of the separation distance r. The results for $N_b = 216$ and $N_b = 54$ are superposed in (b) and (c) respectively.

repel slightly ($V_r > 0$) when they are aligned horizontally. $P(V_r > 0)$ tends towards 0.5 as r increases and the number of bubble pairs considered becomes larger. However, a clear spatial correlation between the radial relative velocities remains visible for $N_b = 216$ and $r = 24a$ and for $\alpha = 2\%$ and $r = 12a$.

Attraction for vertically aligned pairs is consistent with the Navier–Stokes simulation results of Yuan & Prosperetti (1994), with the experimental results of Cartellier & Rivière (2001), and with the drafting, kissing and tumbling mechanism of Fortes *et al.* (1987). Yuan & Prosperetti (1994) determined the equilibrium distance betweeen two bubbles in line as a function of the Reynolds number. For $Re = 20$, they found $r \approx 2.6a$, although they estimate this distance to be too small to be computed reliably by their method. At larger distances, the bubbles attract due to the wake effect. This is very clearly seen in the most dilute case, $\alpha = 2\%$, for $r = 4a$ and θ close to 0 and π. A computer animation of the bubble motion for $\alpha = 2\%$ shows no clear occurrence of bubbles being close enough that they are repelled. When two bubbles approach vertically, the trailing bubble gradually slows down and the two bubbles tumble. For higher void fractions, situations where two close bubbles are aligned vertically and are separated by a distance less than the equilibrium distance occur more frequently. This leads to larger values of $P(V_r > 0)$ at θ close to 0 and π.

For $\alpha \geqslant 6\%$, the results show a weak preference for horizontally aligned bubbles

to repel. This is consistent with the numerical simulation results of Legendre & Magnaudet (1998) in the same range of Reynolds numbers. However, a small valley is seen at $\theta = \pi/2$ for $\alpha = 2\%$. We verified the existence of this valley for a number of values of $r < 8a$. It indicates that bubble pairs that are aligned exactly horizontally have a weak tendency to attract in this dilute case. This tendency is not seen in any other simulation and $P(V_r > 0)$ is greater than 0.5 for bubble pairs at an orientation slightly greater or smaller than $\pi/2$.

These results are qualitatively different from the potential flow calculations of Biesheuvel & van Wijngaarden (1984) and van Wijngaarden (1993). When the boundary layer and the wake effects of the bubbles are neglected, bubbles tend to attract for $\theta = \pi/2$ and repel for $\theta = 0$ and π regardless of the separation distance. Even though potential flow theory correctly predicts that two bubbles align horizontally, the underlying mechanism leading to the side-by-side configuration is fundamentally different from that seen at finite Reynolds numbers. In potential flow, two bubbles that are aligned vertically repel at first, while rotating around each other so that θ tends towards $\pi/2$ (see van Wijngaarden 1993, for example), following which they approach each other along a horizontal line until they touch. At finite Reynolds number, the two bubbles approach along a vertical line, rotate around each other, and repel when they are aligned horizontally, as shown also by Cartellier & Rivière (2001). The difference between potential flow and finite Reynolds number results shows that it is necessary to include the effects of vorticity in the calculation of the motion of bubbles.

$P(V_\theta > 0)$ is plotted versus θ in figure 13 for the same values of r as $P(V_r > 0)$. The general trend is $P(V_\theta > 0) > 0.5$ for $\theta < \pi/2$ and $P(V_\theta > 0) < 0.5$ for $\theta > \pi/2$, confirming that two vertically aligned bubbles tend to rotate around each other and align themselves horizontally. The maximum of $P(V_\theta > 0)$ in $[0, \pi/2]$ is usually not at $\theta = 0$ but at a slightly larger value. This is consistent with the observations made earlier that two bubbles in an in-line configuration approach each other vertically and that there exists an equilibrium position for two bubbles in line, even though this equilibrium position is unstable to lateral displacements. $P(V_\theta > 0)$ tends towards 0.5 faster than $P(V_r > 0)$ when r increases, indicating that the angular relative velocities are less correlated than the radial relative velocities at large distances.

A common feature of most of the curves in figure 13 is that $P(V_\theta > 0)$ is slightly lower than 0.5 in a small interval around $\theta \approx \pi/3$. This can be seen particularly clearly at $\alpha = 2\%$ for $r = 4.0a$ and $5.0a$. At $\alpha = 6\%$ and 12%, this undershoot can also be seen for $r = 4.0a$, but it is smaller. $P(V_\theta > 0) < 0.5$ for θ close to $\pi/2$ means that two bubbles whose line of centres is nearly horizontal but not exactly horizontal tend to rotate around each other away from the horizontal axis. This is somewhat surprising and contrary to the arguments made before. We attribute this phenomenon to the effects of multiple bubble interactions. Consider for example bubble k, located above bubble j in figure 9. The interaction of its wake with bubble j results in an upward motion of bubble j with respect to bubble i and a departure from the horizontal alignment for the bubble pair ij.

To verifiy the sensitivity of the results to the number of discretization intervals Δr and $\Delta\theta$, $G(r)$, $G(\theta)$, $P(V_r > 0)$, and $P(V_\theta > 0)$ are plotted in figure 14 for the worst cases, which are $N_b = 27$, $\alpha = 24\%$ for $G(r)$ and $N_b = 27$, $\alpha = 2\%$ for $G(\theta)$, $P(V_r > 0)$, and $P(V_\theta > 0)$. Differences can be noticed, particularly in $G(\theta)$ and $P(V_r > 0)$ at $r = 4.0a$ when the number of $\Delta\theta$ intervals is doubled, but they can be attributed to the small number of samples due to the small system size.

Likewise, it can be seen that the effect of system size on the microstructure results

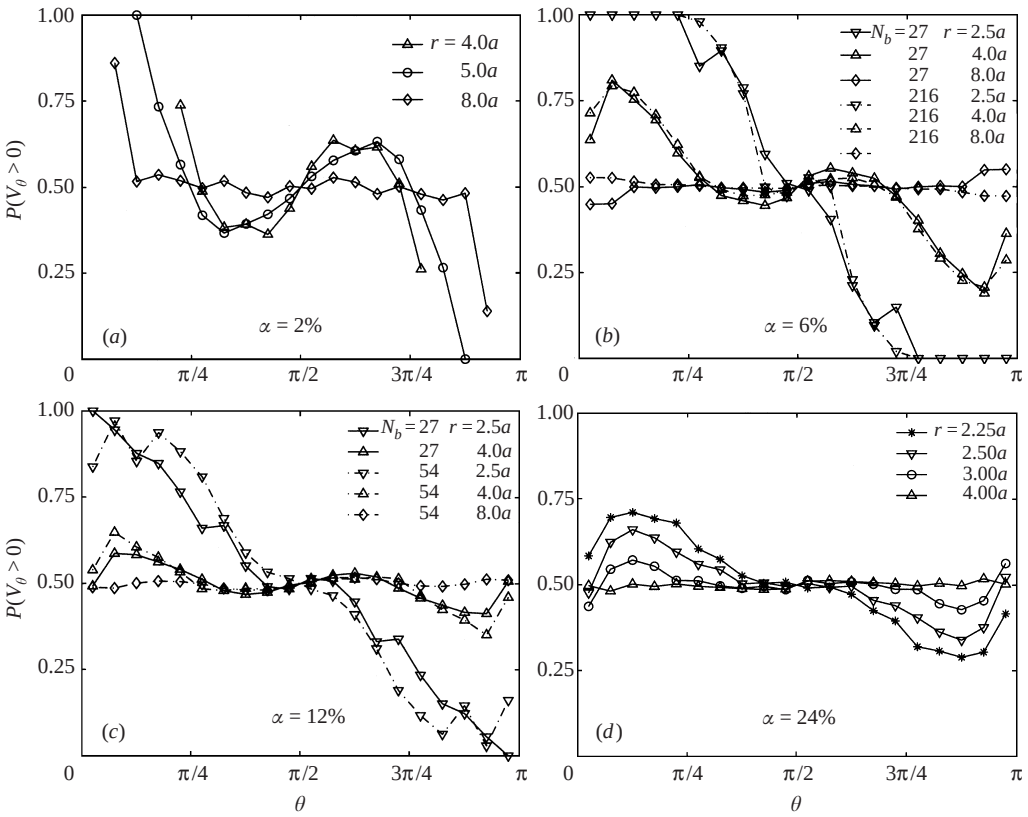

FIGURE 13. $P(V_\theta > 0)$, the probability that the angular relative velocity between two bubbles is positive, as a function of θ for $\alpha = 2\%$, 6%, 12% and 24% and $N_b = 27$ and different values of the separation distance r. The results for $N_b = 216$ and $N_b = 54$ are superposed in (b) and (c) respectively.

is small. Figures 10–13 include results for $N_b = 27$, 91 and 216 at $\alpha = 6\%$ and for $N_b = 27$ and 54 at $\alpha = 12\%$. The effect of system size is most clearly felt in $P(V_r > 0)$, particularly for θ close to 0 and π, and in the peak of $G(\theta)$ at $\theta = \pi/2$, $r = 2.5a$, and $\alpha = 6\%$, but it is otherwise small enough that it does not affect the results. The effect of system size on the microstructure can be quantified by looking at two statistical quantities. The first is the average of $G(r, \theta)$ over a spherical shell of radius r and volume V and over time. The second is the average of $G(r, \theta)$ weighted by the second Legendre polynomial, $P_2^0 = 3\cos^2\theta - 1$ (Ladd 1997). Formally,

$$\langle G \rangle = \frac{1}{T}\int_T \frac{1}{V}\int_V G(r,\theta)\,\mathrm{d}V, \quad \langle A \rangle = \frac{1}{T}\int_T \frac{1}{V}\int_V G(r,\theta)P_2^0(\cos\theta)\,\mathrm{d}V. \tag{3.10}$$

If uniformly distributed point particles were considered, we would have $\langle G \rangle = 1$ and $\langle A \rangle = 0$. $\langle A \rangle = -0.5$ is the limiting case where all bubble pairs are horizontal. Since the bubbles in these simulations have finite size, $\langle G \rangle$ is smaller than 1.0 because of excluded volume effects, but should tend towards 1.0 as r becomes large. $\langle G \rangle$ and $\langle A \rangle$ are shown in figure 15 for $N_b = 12$, 27, 91 and 216. $\langle G \rangle$ does not depend significantly on N_b, while $\langle A \rangle$ increases slightly, indicating that the bubbles are more likely to be aligned horizontally in small systems than in large systems, which is consistent with the small increase in the rise velocity with N_b seen in figure 8(a).

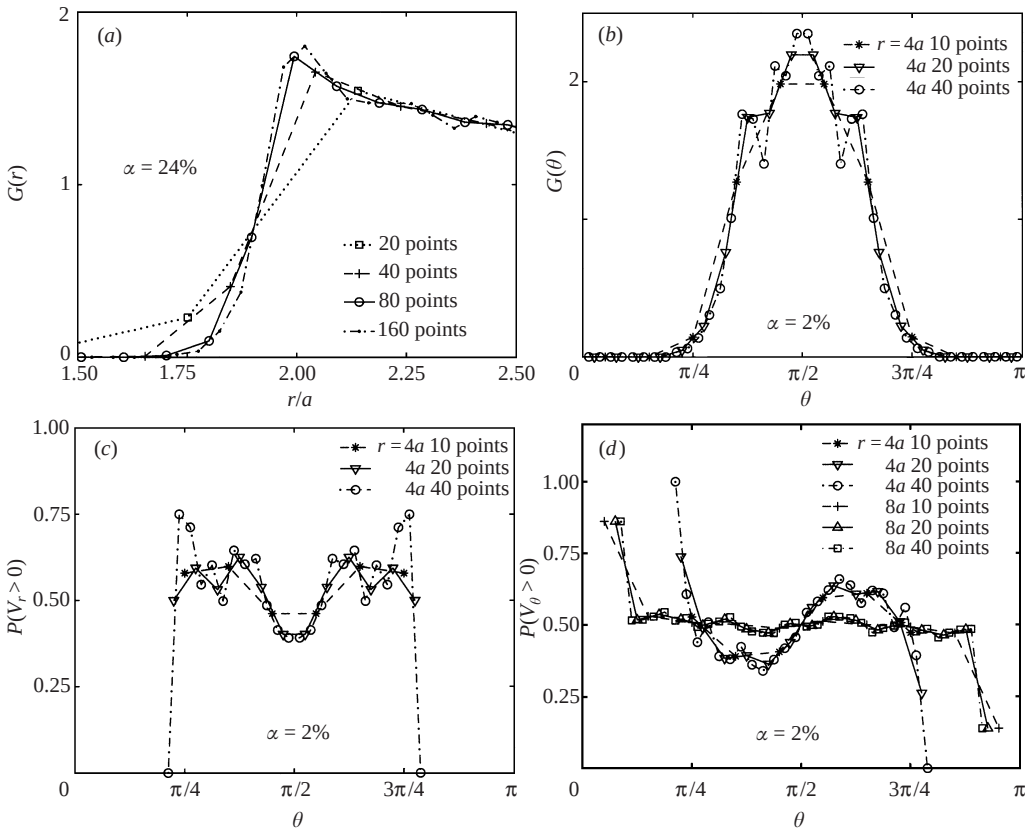

FIGURE 14. Sensitivity test for $G(r)$, $G(\theta)$, $P(V_r > 0)$ and $P(V_\theta > 0)$ to the number of discretization intervals Δr and $\Delta\theta$.

The influence of the microstructure on the rise velocity is further illustrated in figure 16, where the rise velocity of bubble pairs is plotted versus θ. The average rise velocity is also shown by a horizontal solid line. The difference between the average pair velocity and the average velocity, $\Delta W(\theta)$, is positive for θ close to 0 and π and negative for θ close to $\pi/2$, showing that bubble pairs that are aligned vertically rise faster than the average while bubble pairs that are aligned horizontally rise slower. $\Delta W(\theta)$ is not symmetric with respect to the W_d line. In particular for $\alpha = 2\%$ and 6%, the absolute value of $\Delta W(0) = \Delta W(\pi)$ is considerably larger than the absolute value of $\Delta W(\pi/2)$, suggesting that the probability density function of the vertical velocity is also asymmetric, as will indeed be seen in § 3.2 of Part 2.

Computer animations of the simulation results show that the different systems exhibit qualitatively very different behaviors depending on the void fraction. In the most dilute case, $\alpha = 2\%$, the bubbles interact infrequently with their neighbours so that their trajectories are essentially straight, and interactions occur mostly between pairs of bubbles. In addition, the bubbles rarely collide, which is consistent with the findings of Cartellier & Rivière (2001) for clean bubbles. In contrast, in the densest case, $\alpha = 24\%$, strong collective motions involving large numbers of bubbles are observed. It is seen that horizontal rafts of bubbles separated by regions of liquid are repeatedly being formed and broken. The horizontal rafts form through the suction of bubbles located below the raft. They break up when one or more bubbles escape

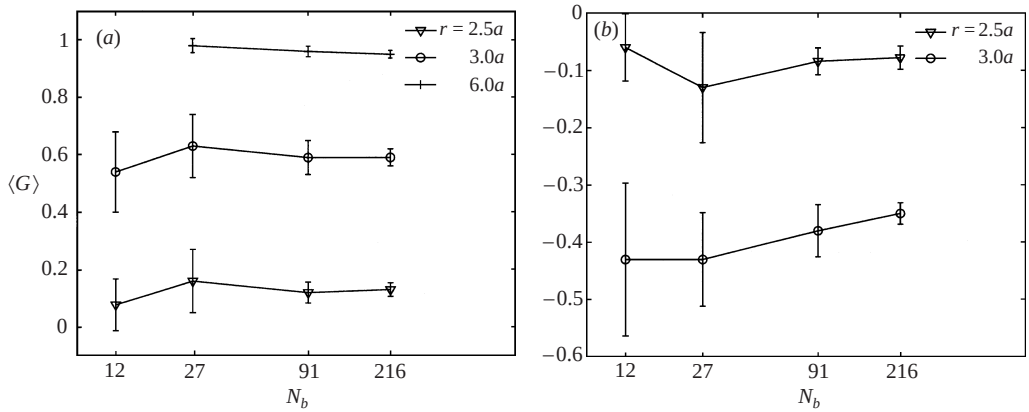

FIGURE 15. Effect of system size on the mean values of (*a*) $\langle G(t)\rangle$ and (*b*) $\langle G(t)\rangle$ at $\alpha = 6\%$.

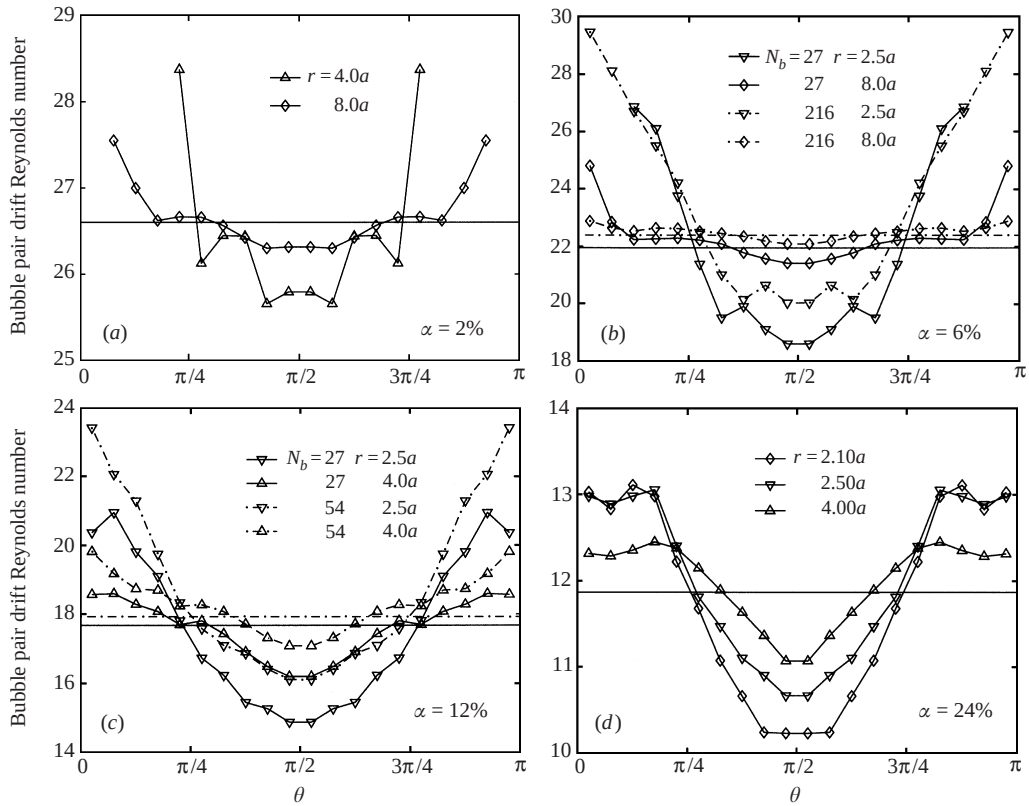

FIGURE 16. The average drift Reynolds number of two bubbles as a function of θ for $\alpha = 2\%$, 6%, 12% and 24% and for different values of the separation distance r. The horizontal solid lines mark the average drift Reynolds numbers for $N_b = 27$, the horizontal dashdot lines mark the average drift Reynolds number for (*b*) $N_b = 216$ and (*c*) $N_b = 54$. The average drift Reynolds numbers have the same values as in figure 8.

the raft and entrain additional bubbles in their wakes. A sequence of plots of the 27 bubbles and eight periodic images is shown in figure 17. It illustrates the transition from the layered state to the homogenously distributed state. The horizontal alignment maximizes the drag since it offers the largest resistance to the flow. There is therefore

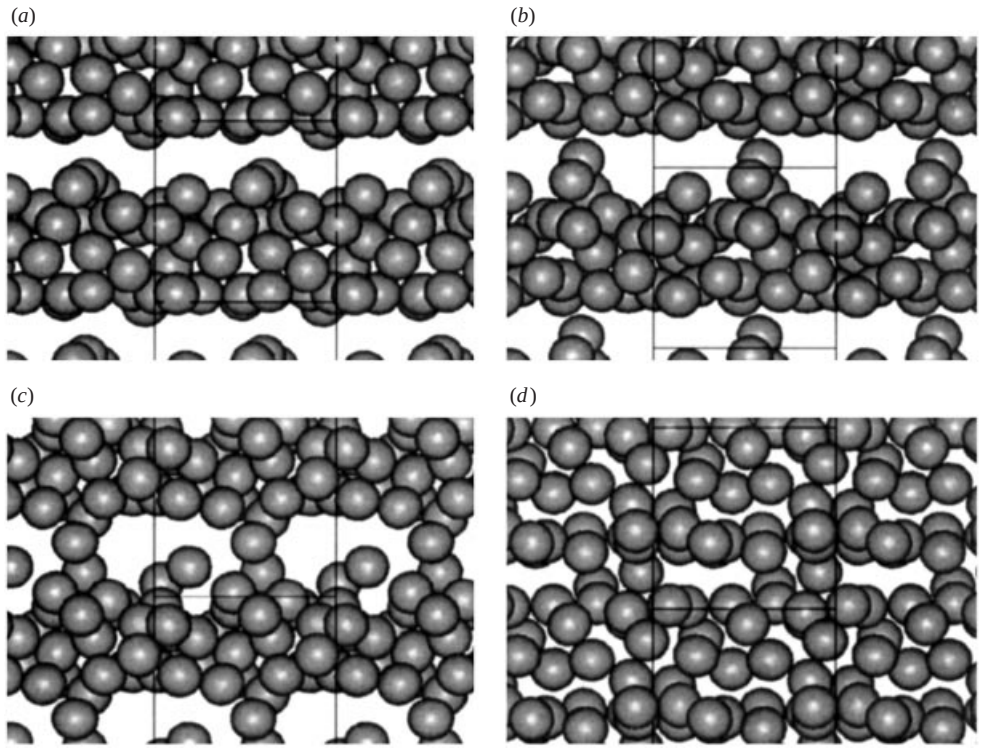

FIGURE 17. The 27 bubbles at $\alpha = 24\%$ and eight periodic images at times (*a*) 141.3, (*b*) 143.0, (*c*) 144.7, and (*d*) 151.9. The bubbles are shown in their frame of reference. The edges of the periodic domain are marked by black lines and illustrate the average upward motion of the bubbles.

an excellent correlation between the times when the horizontal rafts exist and the rise velocity is low in figure 7. Between $t = 0$ and $t = 226$, the process is repeated 11 times. The animation also reveals the presence of cross-stream arrays of bubbles whose velocity is lower than the average velocity and which therefore fall relative to the average bubble phase, and of vertical bubble pairs which accelerate relative to the average bubble phase and undergo drafting, kissing, and tumbling. The overall picture of the flow is very similar to that described by Fortes *et al.* (1987) from their experiments with fluidized solid spheres at similar volume fractions but much higher Reynolds numbers. The existence of falling cross-stream arrays and of rising pairs of drafting bubbles is also seen for $\alpha = 12\%$, but the formation of horizontal layers is not seen as clearly as for $\alpha = 24\%$.

Horizontal rafts were also observed in potential flow simulations (Sangani & Didwania 1993; Smereka 1993; Yurkovetsky & Brady 1996). However, there are fundamental differences between the horizontal rafts seen at finite Reynolds numbers and in potential flow. The following discussion explains these differences and at the same time summarizes the basic two-bubble mechanisms, which, according to our interpretation of the results presented in this section, determine the interaction of bubbles. In potential flow, two vertically aligned bubbles always repel and two horizontally aligned bubbles always attract, regardless of their separation distance. Therefore, the only equilibrium configuration is when the two bubbles are side by side and touch, which results in the formation of permanent horizontal rafts. In contrast, at finite Reynolds numbers, the interplay of viscous and inviscid effects leads to two

equilibrium configurations, one vertical and unstable and the other horizontal and stable. When the separation between two vertically aligned bubbles is large, they attract each other due to the wake effect until they reach an equilibrium separation distance, where the potential effect balances the wake effect. This separation distance increases as *Re* increases (Yuan & Prosperetti 1994). For our value of *Re*, the separation distance is approximately 2.6*a*, implying that vertically aligned bubbles usually attract each other. However, the vertical alignment is unstable. If disturbed, the two bubbles will rotate around each other and move to a horizontal alignment. In the horizontal alignment, the two bubbles attract each other when they are far from each other due to inviscid effects and repel each other when they are close due to viscous effects (Legendre & Magnaudet 1998). The equilibrium separation distance decreases when *Re* increases. The horizontal equilibrium is stable, which explains the preference for bubble pairs to be aligned horizontally and, for $\alpha = 24\%$, the formation of horizontal rafts. However, the horizontal rafts are only temporary. Due to the attraction between vertically aligned bubbles, the rafts break up immediately after they form.

4. Conclusion

The motion of buoyant bubbles in a homogeneous flow is studied by direct numerical simulations, where the effects of viscosity, inertia, interface deformation, and surface tension are all accounted for. The bubbles can deform but remain nearly spherical for the parameters used here. The rise Reynolds number is 12–30, depending on the void fraction, which varies between 2% and 24%. This part focuses on the rise velocity and the microstructure of the bubbles; the dispersion process of the bubbles and the turbulence of the liquid phase are examined in Part 2. The major observations and conclusions are as follows:

(i) A good estimate of the mean drift velocity of the bubbles can be achieved with only 12 bubbles. Likewise, the effect of system size on the microstructure is small when $N_b \geqslant 12$.

(ii) As the void fraction α increases, the drift velocity of the bubbles decreases from 26.60 for $\alpha = 2\%$ to 11.87 for $\alpha = 24\%$. In particular, there is a sharp drop between the drift velocity at $\alpha = 0$ and the drift velocity at $\alpha = 2\%$. A similar observation is made in the experimental study of van Wijngaarden & Kapteyn (1990) at higher Reynolds numbers.

(iii) An analysis of the microstructure reveals a preference for pairs of bubbles to be aligned horizontally. This is consistent with potential flow theory. However, the dynamics of bubble–bubble interactions are markedly different from potential flow predictions. In our simulations, two bubbles that are aligned vertically attract each other due to the wake effect, rotate around each other, and then repel when they are aligned horizontally. This mechanism is similar to the 'drafting, kissing, and tumbling' mechanism of Fortes *et al.* (1987).

(iv) At $\alpha = 24\%$, we observe the periodic formation of horizontal rafts of bubbles separated by liquid. These rafts are not stable and break up when one bubble leaves the rafts and entrains other bubbles behind it. A similar phenomenon has been seen in the sedimentation of spheres in fluidized beds at the same packing fraction (Fortes *et al.* 1987).

(v) While simulations of regular arrays do not provide any information on the microstructure, they can be used to determine rough estimates of the average rise velocity of the bubbles at high void fractions.

The authors gratefully acknowledge the support of the National Science Foundation under grant CTS-9503208 and of the University of Michigan through a Rackham Predoctoral Fellowship. This research was supported in part by NSF cooperative agreement ACI-9619020 through computing resources provided by the National Partnership for Advanced Computational Infrastructure at the University of Michigan Center for Parallel Computing. In addition, this research, in part conducted at the Maui High Performance Computing Center, was sponsored in part by the Air Force Research Laboratory, Air Force Materiel Command, USAF, under cooperative agreement number F29601-93-2-0001. The views and conclusions contained in this document are those of the authors and should not be interpreted as necessarily representing the official policies or endorsements, either expressed or implied, of the Air Force Research Laboratory, the US Government, The University of New Mexico, or the Maui High Performance Computing Center.

REFERENCES

Bhaga, D. & Weber, M. E. 1981 Bubbles in viscous liquids: shapes, wakes, and velocities. *J. Fluid Mech.* **105**, 61–85.

Biesheuvel, A. & van Wijngaarden, L. 1982 The motion of pairs of gas bubbles in a perfect fluid. *J. Engng Maths* **16**, 349–365.

Bunner, B. & Tryggvason, G. 1999 A parallel front-tracking method for the simulation of dispersed multiphase flows. In *Proc. Ninth SIAM Conf. on Parallel Processing for Scientific Computing, San Antonio*.

Bunner, B. 2000 Numerical simulation of gas-liquid bubbly flows. PhD Thesis, The University of Michigan.

Bunner, B. & Tryggvason, G. 2002*a* Dynamics of homogeneous bubbly flows. Part 2: Velocity fluctuations. *J. Fluid Mech.* **466**, 53–84.

Bunner, B. & Tryggvason, G. 2002*b* Effect of bubble deformation on the stability and properties of bubble flows. Submitted to *J. Fluid Mech.*

Cartellier, A. & Rivière, N. 2001 Bubble-induced agitation and microstructure in uniform bubbly flows at small to moderate particle Reynolds numbers. *Phys. Fluids* **13**, 2165–2181.

Clift, R., Grace, J. R. & Weber, M. E. 1978 *Bubbles, Drops, and Particles*. Academic.

Delhaye, J. M. 1974 Jump Conditions and entropy sources in two-phase systems. Local instant formulation. *Intl J. Multiphase Flow* **1**, 393–409.

Drew, D. A. 1983 Mathematical modeling of two-phase flow. *Annu. Rev. Fluid Mech.* **15**, 261–291.

Duineveld, P. C. 1995 The rise velocity and shape of bubbles in pure water at high Reynolds number. *J. Fluid Mech.* **292**, 325–332.

Elghobashi, S. E. & Truesdell, G. C. 1992 Direct simulation of particle dispersion in decaying isotropic turbulence. *J. Fluid Mech.* **242**, 655–700.

Esmaeeli, A. & Tryggvason, G. 1996 An inverse energy cascade in two-dimensional, low Reynolds-number bubbly flows. *J. Fluid Mech.* **314**, 315–330.

Esmaeeli, A. & Tryggvason, G. 1998 Direct numerical simulations of bubbly flows. Part 1. Low Reynolds number arrays. *J. Fluid Mech.* **377**, 313–345.

Esmaeeli, A. & Tryggvason, G. 1999 Direct numerical simulations of bubbly flows. Part 2. Moderate Reynolds number arrays. *J. Fluid Mech.* **385**, 325–358.

Fan, L. S. & Tsuchiya, K. 1990 *Bubble Wake Dynamics in Liquids and Liquid Solid Suspensions*. Butterworth-Heinemann.

Feng, J., Hu, H. H. & Joseph, D. D. 1994 Direct simulation of initial value problems for the motion of solid bodies in a Newtonian fluid. Part 1. Sedimentation. *J. Fluid Mech.* **261**, 95–134.

Fortes, A. F., Joseph, D. D. & Lundgren, T. S. 1987 Nonlinear mechanics of fluidization of beds of spherical particles. *J. Fluid Mech.* **177**, 467–483.

Glowinski, R., Pan, T.-W., Hesla, T. I. & Joseph, D. D. 1999 A distributed Lagrange multiplier/fictitious domain method for particulate flows. *Intl J. Multiphase Flow* **25**, 755–794.

Harper, J. F. 1970 On bubbles rising in line at large Reynolds numbers. *J. Fluid Mech.* **41**, 751–758.

Hetsroni, G. 1982 *Handbook of Multiphase Systems*. McGraw Hill.

Ishii, M. 1975 *Thermo-fluid Dynamic Theory of Two-phase Flows*. Eyrolles.

Ishii, M., Chawla, T. C. & Zuber, N. 1976 Constitutive equation for vapor drift velocity in two-phase annular flow. *AIChE J.* **22**, 283–289.

Ishii, M. & Zuber, N. 1979 Drag coefficient and relative velocity in bubbly, droplet or particulate flows. *AIChE J.* **25**, 843–855.

Jan, Y. J. 1994 Computational studies of bubble dynamics. PhD Thesis, The University of Michigan.

Katz, J. & Meneveau, C. 1996 Wake-induced relative motion of bubbles rising in line. *Intl J. Multiphase Flow* **22**, 239–258.

Koch, D. L. & Ladd, A. J. C. 1997 Moderate Reynolds number flows through periodic and random arrays of aligned cylinders. *J. Fluid Mech.* **349**, 31–66.

Kok, J. B. W. 1989 Dynamics of gas bubbles moving through a liquid. Thesis, University of Twente.

Ladd, A. J. C. 1993 Dynamical simulations of sedimenting spheres. *Phys. Fluids* A **5**, 299–310.

Ladd, A. J. C. 1997 Sedimentation of homogeneous suspensions of non-Brownian spheres. *Phys. Fluids* **9** (3), 491–499.

Lafaurie, B., Nardone, C., Scardovelli, R., Zaleski, S. & Zanetti, G. 1994 Modelling merging and fragmentation in multiphase flows with SURFER. *J. Comput. Phys.* **113**, 134–147.

Lamb, H. 1932. *Hydrodynamics*. Dover.

Legendre, D. & Magnaudet, J. 1998 Interaction between two spherical bubbles rising side by side. In *Proc. Third Intl Conf. on Multiphase Flow, ICMF'98, Lyon, France*.

Loewenberg, M. & Hinch, E. J. 1996 Numerical simulation of a concentrated emulsion in shear flow. *J. Fluid Mech.* **321**, 395–419.

Maxworthy, T., Gnann, C., Kürten, M. & Durst, F. 1996 Experiments on the rise of air bubbles in clean viscous liquids *J. Fluid Mech.* **321**, 421–441.

McLaughlin, J. B. 1996 Numerical simulation of bubble motion in water. *J. Colloid Interface Sci.* **184**, 614–625.

Nguyen, A. V. 1998 Prediction of bubble terminal velocities in contaminated water. *AIChE J.* **44**, 226–230.

Nobari, M. R., Jan, Y.-J. & Tryggvason, G. 1996 Head-on collision of drops – A numerical investigation. *Phys. Fluids* **8**, 29–42.

Nott, P. R. & Brady, J. F. 1994 Pressure-driven flow of suspensions: simulations and theory. *J. Fluid Mech.* **275**, 157–199.

Oka, H. & Ishii, K. 1999 Numerical analysis on the motion of gas bubbles using level set method. *J. Phys. Soc. Japan* **68**, 823–832.

Peskin, C. S. 1977 Numerical analysis of blood flow in the heart. *J. Comput. Phys.* **25**, 220.

Pozrikidis, C. 1993 On the transient motion of ordered suspensions of liquid drops. *J. Fluid Mech.* **246**, 301–320.

Qian, J. 1997 Droplet and flame dynamics in combustion phenomena. PhD Thesis, Princeton University.

Ryskin, G. & Leal, L. G. 1984 Numerical solution of free-boundary problems in fluid mechanics. Part 2. Buoyancy-driven motion of a gas bubble through a quiescent liquid. *J. Fluid Mech.* **148**, 19–35.

Saffman, P. G. 1973 On the settling speed of free and fixed suspensions. *Stud. Appl. Maths* **LII**, 115–127.

Sangani, A. S., Zhang, D. Z. & Prosperetti, A. 1991 The added mass, Basset, and viscous drag coefficients in nondilute bubbly liquids undergoing small-amplitude oscillatory motion. *Phys. Fluids* A **3**, 2955–2970.

Sangani, A. S. & Didwania, A. K. 1993 Dynamic simulations of flows of bubbly liquids at large Reynolds numbers. *J. Fluid Mech.* **250**, 307–337.

Smereka, P. 1993 On the motion of bubbles in a periodic box. *J. Fluid Mech.* **254**, 79–112.

Spelt, P. D. M. & Sangani, A. S. 1998 Properties and averaged equations for flows of bubbly liquids. *Appl. Sci. Res.* **58**, 337–386.

Squires, K. D. & Eaton, J. K. 1990 Particle response and turbulence modification in isotropic turbulence. *Phys. Fluids* A **2**, 1191–1203.

Tryggvason, G., Bunner, B., Esmaeeli, A., Juric, D., Al-Rawahi, N., Tauber, W., Han, J., Nas, S.

& Jan, Y.-J. 2001 A front tracking method for the computations of multiphase flow. *J. Comput. Phys.* **169**, 708–759.

Unverdi, S. O. & Tryggvason, G. 1992 A front-tracking method for viscous, incompressible, multi-fluid flows. *J. Comput. Phys.* **100**, 25–37.

Wang, L.-P. & Maxey, M. R. 1993 Settling velocity and concentration distribution of heavy particles in homogeneous isotropic turbulence. *J. Fluid Mech.* **256**, 27–68.

van Wijngaarden, L. 1993 The mean rise velocity of pairwise-interacting bubbles in liquid. *J. Fluid Mech.* **251**, 55–78.

van Wijngaarden, L. & Kapteyn, C. 1990 Concentration waves in dilute bubble/liquid mixtures. *J. Fluid Mech.* **212**, 111–137.

Yuan, H. & Prosperetti, A. 1994 On the in-line motion of two spherical bubbles in a viscous fluid. *J. Fluid Mech.* **278**, 325–349.

Yurkovetsky, Y. & Brady, J. 1996 Statistical mechanics of bubbly liquids. *Phys. Fluids* **8**, 881–895.

Zenit, R., Koch, D. L., & Sangani, A. S. 2001 Measurements of the average properties of a suspension of bubbles rising in a vertical channel. *J. Fluid Mech.* **429**, 307–341.

Zhou, H. & Pozrikidis, C. 1993 The flow of ordered and random suspensions of two-dimensional drops in a channel. *J. Fluid Mech.* **255**, 103–127.